AN OPTOELECTRONIC SYSTEM FOR DEVICE LOCALIZATION IN INTERVENTIONAL MRI

by

Murat Tümer

B.S., in EE, Boğaziçi University, 2004

M.S., in BME, Boğaziçi University, 2007

Submitted to the Institute of Biomedical Engineering

in partial fulfillment of the requirements

for the degree of

Doctor

of

Philosophy

Boğaziçi University

2015

ACKNOWLEDGMENTS

I am really thankful to my advisor Prof. Cengizhan Öztürk for his support throughout this study, and Prof. Yekta Ülgen. I also want to thank Baykal Sarıoğlu for his efforts throughout this project and Berk for his help before/during/after the experiments. Last but not least, people at Biomedical, thank you all for your friendship, and occasional grill and fish parties making me happy and fresh every time. And a special thank goes to my family for their moral support during this long period of time.

This study was supported by The Scientific and Technological Research Council Of Turkey (TÜBİTAK, Project 111E197) and Boğaziçi University LifeSci Center (Ministry of Development, 2009K1200520), The experiments were conducted at UMRAM (National Magnetic Resonance Research Center) at Bilkent University, Ankara and Acıbadem Kozyatağı Hospital, Istanbul.

ABSTRACT

AN OPTOELECTRONIC SYSTEM FOR DEVICE LOCALIZATION IN INTERVENTIONAL MRI

In active catheter tracking, a microcoil directly connected to the MRI system and positioned at the distal end of the catheter is employed for localization. The peaks in the frequency spectrum of the acquired MR signal correspond to catheter's physical location. The major problem with active techniques is the RF heating due to long conducting wires. Fully optical systems that replace the conducting wires with inherently RF-safe optical fibers are proposed. In these systems, the SNR suffers from the electro-optical signal conversion distally (and opto-electrical conversion proximally) at this high frequency. Amplifying and frequency down-converting the MR signal at the catheter tip could minimize signal losses. Amplification could be achieved with an LNA placed next to the microcoil. To provide the reference signal to the mixer for frequency down-conversion of the amplified MR signal, an outside generator or on-chip oscillator could be used. Both methods have their disadvantages like increased complexity at the distal end due to additional cable and frequency drift over time due to temperature or bias voltage variations.

In this work, the reference signal for frequency down-conversion is provided from the MRI scanner's own transmitter! It is a very reliable source of signal since no frequency drift for the transmitter is expected over a specific imaging sequence interval. The frequency of the reference signal is defined as an offset with respect to the center frequency of the scanner, making this technique immune to main field drifts. Following down-conversion, the electrical signal is converted into optical signal for MR-safe transmission. This is also critical to protect the circuitry of the distal unit and receiver from currents that would be induced on the outer surface of the cable.

Keywords: interventional MRI, device localization, catheter tracking, optoelectronics.

ÖZET

GİRİŞİMSEL MR'DA CİHAZ TAKİBİ İÇİN OPTOELEKTRONİK BİR SİSTEM

Aktif kateter takibinde, konum belirlemek için kateterin distal ucunda bulunan ve MR sistemine bağlı bir mikro bobin kullanılır. Topladığı MR sinyallerinin frekans spektrumundaki tepe değerleri fiziksel konumlara karşılık gelmektedir. Aktif yöntemlerdeki ana sorun, uzun kablolar nedeniyle meydana gelen RF'e bağlı ısınmadır. Bu kabloların yerine, doğası gereği MR uyumlu olan fiber optik kablolar kullanılmasını sağlayan optik sistemler önerilmiştir. Ancak bunlarda elektriksel sinyalin optiğe, daha sonra optiğin de yine elektriksel sinyale çevrilmesi sırasında meydana gelen kayıplar nedeniyle sinyal gürültü oranı düşük olmaktadır. MR sinyalini iletmeden önce daha kateterin ucunda kuvvetlendirmek ve frekansını düşürmek sinyal kayıplarını düşürmeye yarayabilir. Kuvvetlendirme, distal uçta bobinin yakınına yerleştirilen bir LNA ile yapılabilir. Frekans düşürme işlemi için referans sinyal dışarıdaki bir üreteçten ya da LNA ile aynı çipe yerleştirilmiş bir osilatörden alınabilir. İki yöntemin de ekstra kablo gereği nedeniyle distal uçta karmaşıklığı artırmak ve sıcaklık ya da giriş öngerilimindeki oynamalar nedeniyle meydana gelen frekans kaymaları gibi dezavantajları vardır.

Bu çalışmada frekans düşürme işlemi için gerekli referans sinyali, MR cihazının kendi vericisinden alınmıştır. Bir görüntüleme sekansı sırasında geçen kısa sürede, frekansta tespit edilebilir bir kayma olması beklenmediğinden ve frekansı MR'ın merkez frekansına olan uzaklığı şeklinde bağıl olarak belirlenebildiğinden, bu verici çok güvenilir bir sinyal kaynağıdır. Elektriksel sinyal, MR güvenli olarak iletim için, frekans düşürme işlemini takiben optiğe çevrilmiştir. Bu, aynı zamanda iki uçtaki devreleri kabloda endüklenebilecek büyük akımlardan korumaya da yardımcı olmaktadır.

Anahtar Sözcükler: girişimsel MR, girişimsel tıbbi cihaz konum belirleme, kateter takibi, optoelektronik.

TABLE OF CONTENTS

LIST OF FIGURES

LIST OF TABLES

LIST OF SYMBOLS

B_0	Main magnetic field
B_1	RF magnetic field
BW	Bandwidth of MR signal
C_S	Power supply capacitor
f_0	Larmor frequency
f_C	Cut-off frequency of the filter
f_{MR}	Frequency of the MR signal
f_{LA}	Frequency of LARFET
f_x	Frequency of the MR signal acquired from location x
f_S	Sampling frequency of the ADC
FA_{sinc}	Flip angle of a sinc shaped RF pulse
FA_{125}	Flip angle of the 125 MHz leaky signal
G	Magnetic field gradient
G_x	Magnetic field gradient along x-axis
L	Signal acquisition time
P_{sinc}	Power of a sinc shaped RF pulse
P_{125}	Power of the 125 MHz leaky signal
T	Duration of the RF pulse
V_f	Forward bias voltage of the diode
γ	Gyromagnetic ratio

LIST OF ABBREVIATIONS

2D	Two-Dimensional
3D	Three-Dimensional
BPF	Band-Pass Filter
CMOS	Complementary Metal-Oxide Semiconductor
CT	Computed Tomography
EPI	Echo-Planar Imaging
DFT	Discrete Fourier transform
DTFT	Discrete-time Fourier transform
HIFU	High-Intensity Focused Ultrasound
IC	Integrated Circuit
iMRI	Interventional Magnetic Resonance Imaging
LARFET	Low Amplitude RF Pulse at Echo Time
LED	Light Emitting Diode
LNA	Low-Noise Amplifier
MR	Magnetic Resonance
MRI	Magnetic Resonance Imaging
NF	Noise Figure
NMR	Nuclear Magnetic Resonance
PCB	Printed Circuit Board
RF	Radio Frequency
rtMRI	Real-Time Magnetic Resonance Imaging
SNR	Signal-to-Noise Ratio
UMC	United Microelectronics Corporation

1. Introduction

1.1 From NMR to MRI

The concept of magnetic resonance can be tracked back to the experiment by Otto Stern and Walther Gerlach in 1922 in Frankfurt, Germany [1]. This experiment proved the theory that particles have a magnetic moment related to their angular momentum and it is quantized in discrete amounts. The Stern-Gerlach apparatus consists of an oven as the emitter of atoms, a slit, an inhomogeneous magnetic field, and a target as shown in Figure 1.1. The silver atoms emitted go through a collimating slit to cut out a narrow beam and are deflected by the inhomogeneous magnetic field. A homogeneous magnetic field would create no net force for deflection. Then at the target two discrete concentration lines are observed, instead of a homogeneous depositing area as shown in Figure 1.2. This indicates that the molecular beam was split into two beamlets by the inhomogeneous magnetic field and consecutively existence of two discrete states of the magnetic moment of the silver atoms. In fact, the observed splitting of the silver beam was due to the spin angular momentum of the unpaired electron of silver atom and not due to particles in the nucleus.

Stern went on to demonstrate and measure the quantized spin of the proton together with the size of its magnetic moment [7, 8] and finally received the Nobel Prize in Physics in 1943 "for his contribution to the development of the molecular ray method and his discovery of the magnetic moment of the proton". Gerlach was omitted by the Prize Community, because he was still active in Nazi Germany, where Stern had already moved to the USA in 1933.

After this discovery, in the 1930's Isidor Rabi and colleagues started experiments to determine spin numbers of different atomic nuclei. In 1937 using an extended version of the Stern-Gerlach apparatus, they discovered that by applying an RF field, the magnetic momentum of the atomic nuclei can be switched from one state to an-

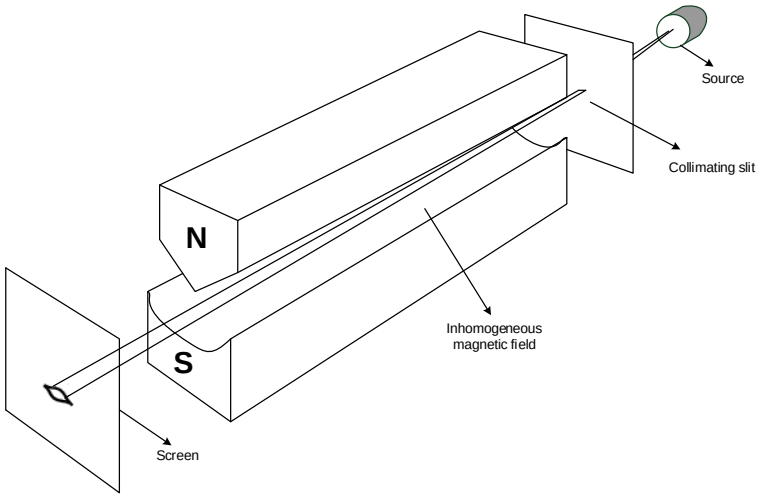

Figure 1.1 The Stern-Gerlach apparatus. The silver atoms emitted from the source go through an inhomogeneous magnetic field where the beam was split into two beamlets indicating two discrete states of the magnetic moment. The result is observed on a glass screen where the deposits formed a pattern.

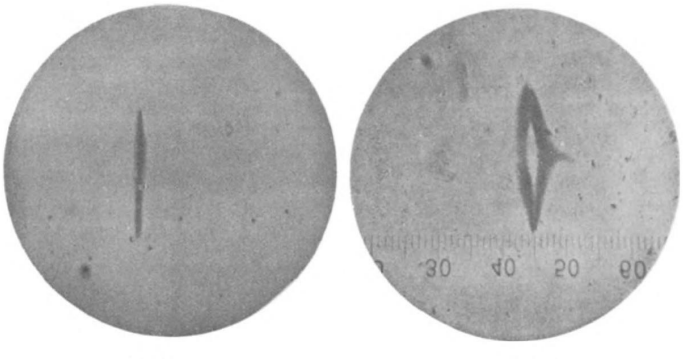

Figure 1.2 The screen captures of the Stern-Gerlach Experiment. **Left:** The screenshot was obtained by 4.5 h exposure without the existence of the magnetic field. The hitting points of the silver atoms on the screen forming a straight line representing the collimating slit used to cut out a narrow beam. **Right:** The screenshot was obtained by 8 h exposure with the magnetic field turned on. The narrow beam was split into two beamlets and hitting points accumulated on two discrete lines instead a single one in the middle. Image taken from Stern's paper published in 1922 [1].

other. The arrangement used in our experiment is shown in Figure 1.3. Molecules are emitted through the slit labeled as O into a high vacuum apparatus. They go through inhomogeneous magnetic fields formed by Magnet A and Magnet B, which have opposite directions and detected by a detector at D. A collimating slit, S, is used for beam selectivity. There is an additional magnet in between, which generates a homogeneous magnetic field and is equipped with an RF coil. RF energy when applied at resonance frequency of the spins may switch the moments from one state to another. The two solid curves indicate the paths of two molecules having different moments and velocities and whose moments are not changed during passage through the apparatus. The two dotted curves in the region of the B magnet indicate the paths of two molecules the projection of whose nuclear magnetic moments along the field has been changed in the region of the C magnet. [2]. This showed that state transitions could be induced by depositing energy to the atomic nuclei using time varying fields or RF fields at a certain frequency called Larmor frequency. With this setup, determination of the magnetic properties of the atomic nuclei by using the resonance frequency was first described and measured by Isidor Rabi in 1938 [9] and he received the Nobel Prize in 1944 "for his resonance method for recording the magnetic properties of atomic nuclei".

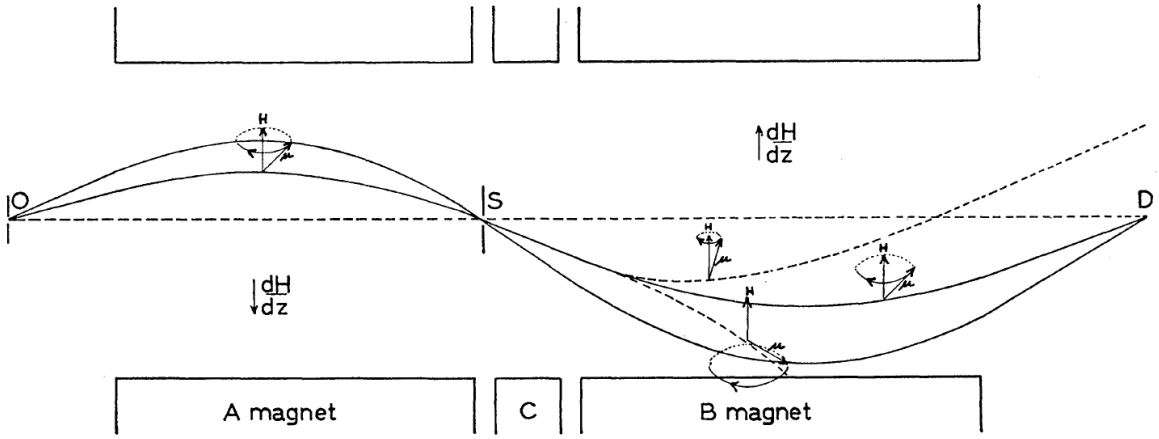

Figure 1.3 The arrangement of Rabi which is an extended version of Stern-Gerlach appartus. Image taken from Rabi's paper published in 1938 [2].

On the other hand, the term nuclear magnetic resonance (NMR) was first introduced by the Dutch physicist Cornelis Jacobus Gorter in a 1942 paper explaining

his failing experiments to detect NMR [10]. However, he played an important role in this discovery by inspiring Rabi with his ideas during a visit in 1936.

The magnetic moment of atomic nuclei and existence of discrete states only was understood. But the experimental setp required a high degree of vacuum to prevent molecular beams colliding with air molecules. In 1946, Felix Bloch and Edward Mills Purcell extended the technique for precision measurement of spins around a magnetic field [3, 11]. They were able to excite spins and record a precessional signal from liquid samples. Bloch and colleagues recognized that the NMR nuclear induction signal they had recorded was a transient phenomenon. Bloch reasoned that the spins would not precess indefinitely around B_0, but would instead return to their initial alignment parallel to B_0 meanwhile releasing energy to the environment, which is basically the origin of the NMR signal [12]. This phenomenon was named relaxation. Many theoretical details were also explained by these two scientists and they shared the Nobel Prize in Physics in 1952 "for their development of new methods for nuclear magnetic precision measurements and discoveries in connection therewith". Their discovery provided researchers with the potential to identify the specific atoms in a solid or liquid in an non-invasive manner.

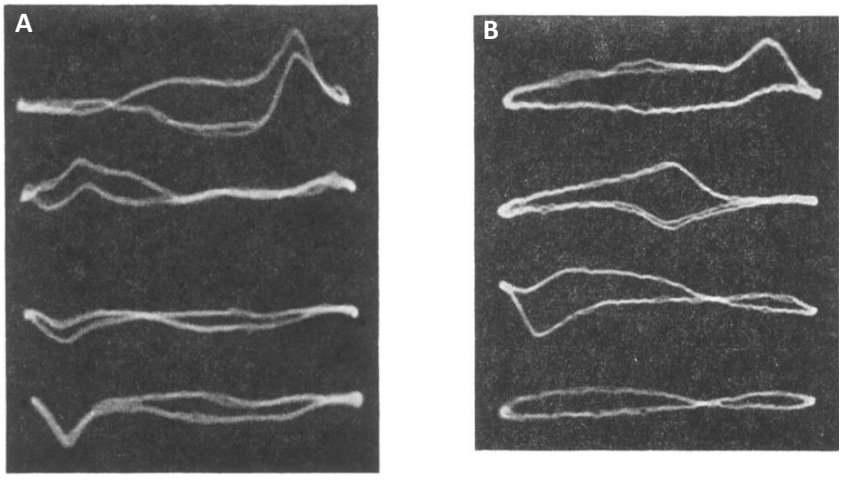

Figure 1.4 Photographic records of proton signals from **A)** water and **B)** paraffin. Bloch et al carried out a continuous wave (CW) NMR experiment where the RF transmit field (B_1) was kept constant as the magnetic field was varied and the system swept through resonance. Images taken from Bloch et al. paper published in 1946 [3].

All these scientists were physicists and the discoveries were in the field of physics.

After the concept of nuclear magnetic resonance was well established and chemical shift was discovered in 1950, commercial spectrometers were introduced into market and the chemists took over. They used the NMR to investigate the chemical properties of molecules. Then chemical shift was discovered which means same atoms precess at slightly different frequencies depending on the atoms they are making chemical bonds. Figure 1.5 shows the first chemical shift [4].

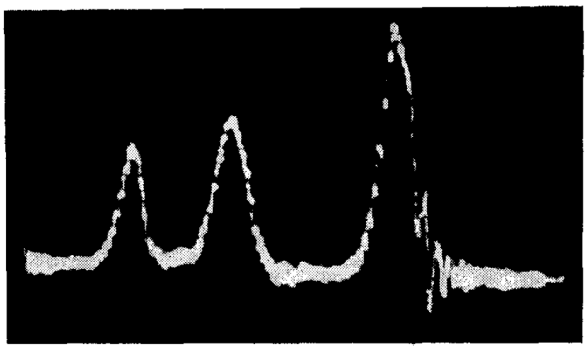

Figure 1.5 Oscillograph trace of the nuclear induction signal from ethyl alcohol. Peaks from left to right represent OH, CH_2, CH_3. Image taken from Arnold et al. paper 1951 [4].

The 50's and 60's were very effective on development of NMR spectroscopy. Richard Robert Ernst developed Fourier-transform NMR in 60's. The signal from spectroscopy devices was very noisy and averaging would help to increase the signal-to-noise ratio (SNR). But a single frequency sweep was taking 2 to 8 min at that time and 100 acquisitions (for an increase of 10 in SNR) were too long to wait. Instead, he proposed to excite all the spins with a non-selective pulse and then recording the composite signal and taking its Fourier transform [13]. Repeating this 100 times and averaging Fourier spectra gave better results. Soon after this discovery FTNMR spectroscopy devices were introduced to market. Richard Robert Ernst pursued his studies on development of multi-dimensional NMR spectroscopy and received the Nobel Prize in Chemistry in 1991 for "for his contributions to the development of the methodology of high resolution nuclear magnetic resonance spectroscopy". Kurt Wüthrich received (1/2 of) the Nobel Prize in Chemistry in 2002 "for his development of NMR spectroscopy for determining the three-dimensional structure of biological macromolecules in solution".

Erik Odeblad from Sweden is the first scientist to use NMR for study of biological samples. After a visit at Bloch's laboratory he got his own NMR spectroscopy device and reported relaxation time differences in NMR signals from different tissues [14]. The fact, that different tissues have distinct relaxation times, is the the phenomenon that explains tissue contrast in MR imaging. Raymond Damadian was the first scientist to observe relaxation time differences for discriminating between malignant tumors and normal tissue [15]. Although his later patented work presented an unfeasible method to obtain spatially selected NMR signals, it motivated the application of NMR in medicine.

The idea of generating an image from the signal of precessing spins at Larmor frequency was introduced by Paul Lauterbur. He used a back projection technique similar to that used in CT (which was introduced by Hounsfield in 1973) and demonstrated imaging of H_2O in small test tubes surrounded by D_2O as shown in Figure 1.6 which was impossible by using any other imaging modality [5]. As stated by the Nobel Prize committee, he discovered the possibility to create a two-dimensional picture by introducing gradients in the magnetic field. Peter Mansfield had already shown use of magnetic field gradients for a spatial separation of NMR signals [16] and later demonstrated imaging [6]. Figure 1.7 shows the first MR image obtained by Mansfield. He also pioneered fast MRI with echo-planar imaging (EPI) and further developed it [17, 18]. Both Lauterbur and Mansfield were awarded with the Nobel Prize in Medicine in 2003 "for their discoveries concerning magnetic resonance imaging". Ernst also contributed to imaging by proposing use of phase and frequency encoding, and the Fourier Transform [19] which is the basis of current MRI techniques.

In years, the word 'nuclear' was dropped from the name of the imaging modality due to widespread concern over any phrase containing it, leaving MRI as the acronym. This shortened name is also appropriate by reflecting that no ionizing radiation is used to generate MR images in contrast to X-ray techniques.

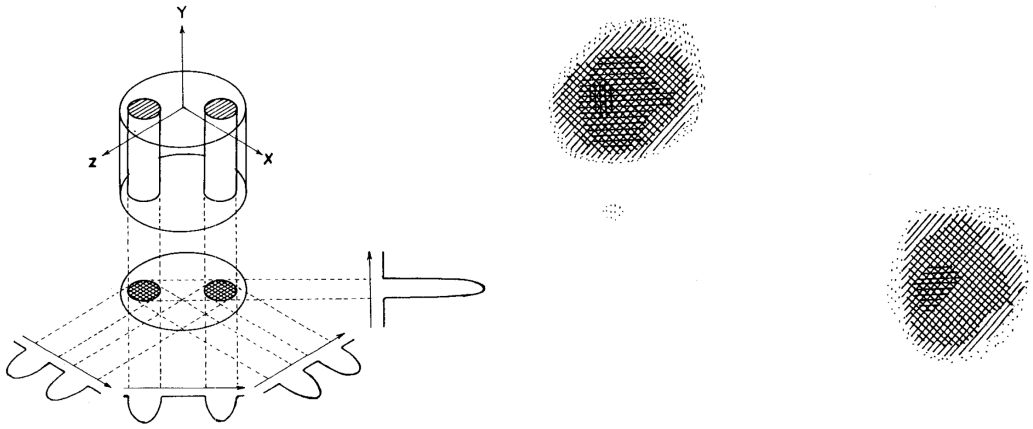

Figure 1.6 The first MR images. **Left:** Two cylinders of H_2O surrounded by D_2O was imaged using backprojection method. **Right:** The MR image of this object obtained using four projections. This method was called zeugmatography by Lauterbur, which means "that which is used for joining". Images taken from Lauterbur's paper 1973 [5].

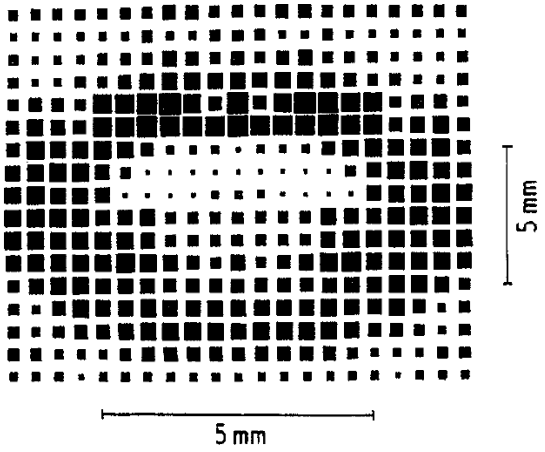

Figure 1.7 2D image of the cross section of a cylindrical annular tube. Image taken from Mansfield's paper 1974 [6].

1.2 Interventional MRI

Interventional MRI is the use of MRI to perform interventional radiology procedures. Among them, endovascular MRI procedures such as cardiac catheterization, invasive imaging of peripheral artery atheromata, selective intraarterial MR angiography, preliminary angioplasty, and stent placement make up the biggest part. Additionally, thermometry, biopsy, ablations, and high-intensity focused ultrasound (HIFU) are also routinely performed under MR guidance.

Fast imaging is essential for MR-guided interventions. Introduction of fast imag-

ing sequences (i.e. real-time imaging)and better hardware (i.e. stronger magnet and faster gradients), and fast imaging techniques such as sparse or partial k-space filling, and parallel imaging enabled the use of this diagnostic imaging modality in interventions and the concept interventional MRI was born. It has been only two decades since the potential of MR-guided endovascular procedures was recognized and iMRI is still an active research area.

1.3 Motivation

MRI as a real-time imaging modality for use during interventional procedures is an active research area. Although the spatial resolution with MRI is not close to that of X-ray methods, more anatomical detail can be visualized because of increased soft-tissue contrast without exposure to ionizing radiation. Temporal resolution in MRI is also lower than that of X-ray techniques but demonstrably sufficient to guide catheterization in humans [20]. MRI is also attractive for flexible slice positioning and its ability to display different tissue contrasts, motion, and flow. Techniques for catheter tracking in MRI can be grouped into three main categories: passive, semi-active, and active methods [21]. Most interventions rely on tracking the interventional device's tip ('tip tracking') either in real-time images or in the coordinate system of the MR scanner [22–25]. Beyond, defining the device tip, visualization of the interventional device's shaft [26,27] may be critical in many clinical scenarios, especially when flexible devices, such as catheters, are navigated. But even with shaft visibility, tracking of tip is crucial for most clinical procedures.

1. **Passive** tracking involves the use of contrast agents or paramagnetic materials to enhance the contrast between the catheter and the surrounding anatomy [28,29]. Despite their simplicity in implementation, the passive methods primarily suffer from low contrast-to-noise ratios, and sometimes the appearance of the marker is indistinguishable from image artifacts [30]. Additionally, the catheter must be manipulated within the imaging plane since no positional coordinates are

generated for automatic scan plane prescription.

2. **Semi-active** techniques are based on local resonant circuits without external connections. Through inductive coupling to the transmit coil, these resonant circuits provide flip angle amplification during RF transmission and signal amplification during reception, resulting in local signal enhancement [26, 31–34]. In these techniques, the coil, and consequently, the catheter tip can be localized by projecting the volume onto orthogonal planes. The signal peak in the projections corresponds to the location of the resonant coil.

3. In **active** catheter tracking, the microcoil is directly connected to the MRI system and is positioned at the distal end of the catheter for localization [35–37]. The peaks in the frequency spectrum of the acquired MR signal correspond to the physical location [38]. It is also useful for signals from device channels to be displayed in color for better visualization [39, 40]. Since this technique provides the location directly, it can also be used in automated catheter tracking, where the imaging plane and imaging parameters are adjusted by the tracking results [41, 42]. Orientation information can also be obtained by using more than one coil [43] or the shaft of the guidewire as a loopless antenna [27].

The major problem with active techniques is RF heating due to long conducting wires [44, 45]. Different methods have been proposed to reduce heating [46–48] or for heating-controlled operation [49] without avoiding the conducting wires. Additionally, fully optical systems were proposed that replace these conducting wires with inherently RF-safe optical fibers, eliminating the risk of RF heating [50, 51]. In these systems, the MR signal is transmitted with all amplitude and phase information, allowing high-resolution imaging besides projection-based tip tracking. In this case, the SNR suffers from the electro-optical signal conversion distally (and opto-electrical conversion proximally) at this high frequency.

Amplifying [52] and frequency down-converting [53, 54] the MR signal at the catheter tip could minimize signal losses and thus provide higher SNR. The mixing signal could be provided from an outside generator, necessitating an additional cable

to transmit this signal to the catheter tip. This would increase the complexity at the distal end. A second alternative is an oscillator placed at the catheter tip next to the low-noise amplifier (LNA), and mixer [53]. But for on-chip oscillators a decrease in accuracy is expected over time due to temperature or bias voltage variations.

2. The LARFET Method

In this work we propose to provide the reference signal for frequency down-conversion from the MRI scanner's own transmitter. Since no frequency drift for the transmitter is expected over a specific imaging sequence interval, it is a very reliable source of signal. A low- amplitude RF pulse applied at echo time (LARFET) is acquired by the antenna (microcoil) and used as the reliable and precise reference to down-convert the echo signal. The frequency of LARFET is defined as an offset with respect to the center frequency of the scanner, making the technique immune to main field drifts. Following down-conversion, the electrical signal is converted into optical signal for MR-safe transmission [55, 56]. This is also critical to protect the circuitry of the distal unit and receiver from currents that would be induced on the outer surface of the cable.

2.1 Materials and Methods

Three pieces of a CT dose index (CTDI) phantom were placed in 12.5 cm intervals as shown in Figure 2.1. On each piece, there are 9 holes in a 3×3 placement with 10.61 cm grid interval, resulting in a 21.22 × 21.22 × 25 cm^3 FoV to investigate and twenty-seven positions in 3D coordinate system. A circuit consisting of an LNA, mixer, and optical transmitter was connected on a 4.3 × 6.3 cm printed circuit board (PCB). The circuitry, which has a total current consumption of 24 mA, was powered from an MR-compatible battery (MP-174565, 4.8 Ah, Saft Batteries, Bagnolet, France). A microcoil ($\varnothing$ = 2 mm, l = 3 mm, and N = 10 turn) was used to acquire the signals. It was immersed in a saline-filled and sealed glass tube (Figure 2.2-A), which fits into the holes very tightly. The 3×3 grid was aligned parallel to the patient table by using a spirit level, and plastic rods (Figure 2.2-B). For each spatial location, an image was first acquired, in which the actual location of the microcoil was detected as a hyper-intense spot, a result of elevated RF flip angle at this location, i.e. using semi-active tracking.

Following this, the location was determined using the new active method, which will be elaborated on in a subsequent section, and compared to the semi-active localization. The instrumentation consisted of two units interconnected by a fiber-optic cable. The

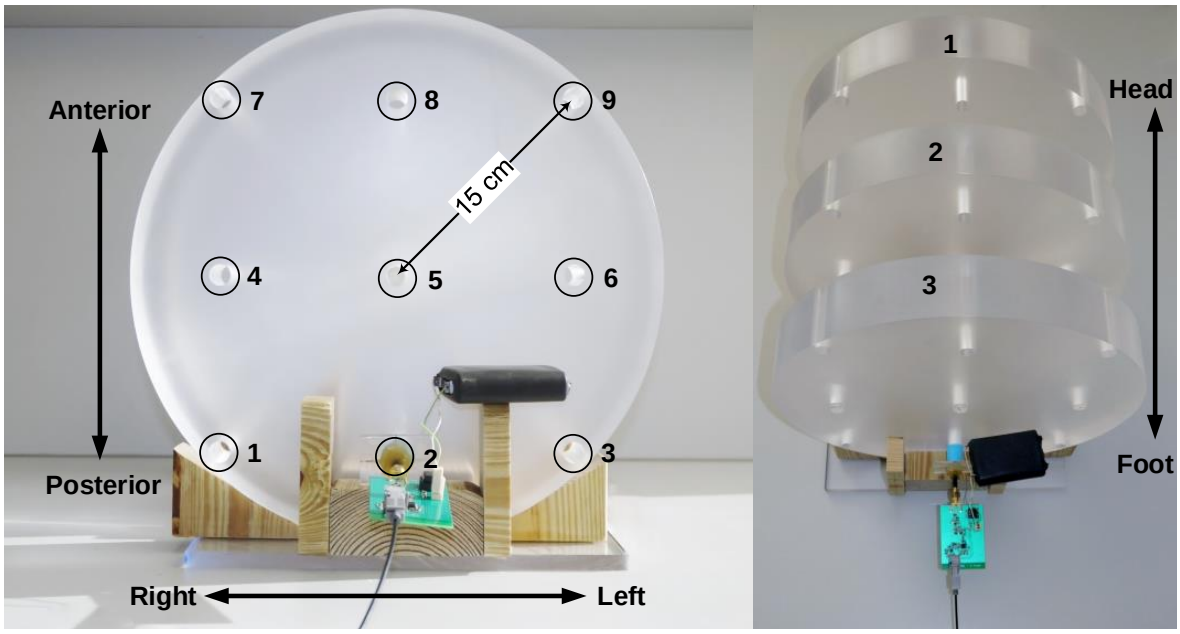

Figure 2.1 The locations for the experiment were selected from the holes already existing on a CTDI phantom consisting of 3 equal pieces. On each of these pieces, there are 9 holes which have a diameter of 1.3 cm and are drilled in 10.61 cm intervals ($1/\sqrt{2}$ of the length of the 15 cm diagonal). They were numbered starting from the lower left corner (reader's view). So the holes on the first, second, and third pieces had the numbers 11 to 19, 21 to 29, and 31 to 39, respectively.

distal portion (Figure 2.2-A) was placed inside the scanner (Siemens Trio, Erlangen, Germany) to acquire the MR signals and the concurrent LARFET signal. The output of this unit was an optical signal and transmitted to an external unit located outside the MR room. The external unit reconverted the optical signal into electrical, which was then digitized and analyzed.

2.1.1 Positional localization MRI pulse sequence

The applied pulse sequence is illustrated in Figure 2.3. It starts with a nonselective RF pulse applied by the body coil to excite all the spins. The amplitude of the RF pulse is a balance between obtaining sufficient tracking SNR, which increases as one approaches the Ernst angle for a given repeat time (TR), and the desire for

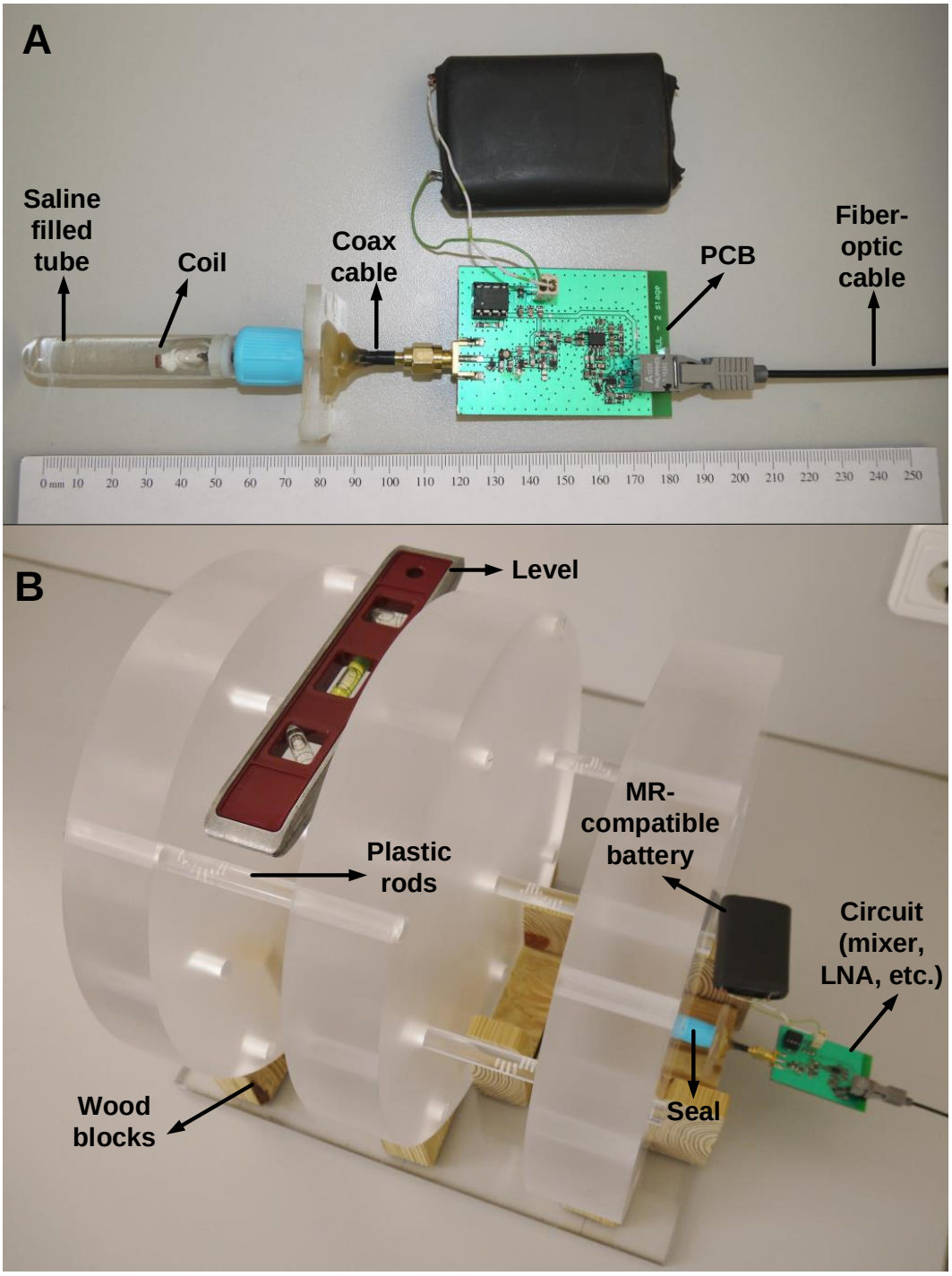

Figure 2.2 **A)** The distal unit. The coil was immersed in a saline-filled and sealed glass tube. It was connected to the PCB via a 7 cm coax cable and an SMA connector. This configuration helped keep the coil outside the no-signal region shielded by the ground plane of the PCB. All stages were connected from discrete components, and at the last stage, the electrical signal was converted to optical by the LED (HFBR-1518). **B)** The part of the experimental setup that was placed inside the scanner. Three pieces that make up a CTDI phantom were fixed using a homemade wooden framework such that the distance between them is 12.5 cm. A level put on plastic rods which were inserted into holes ensured the parallelism of the grid with respect to the patient table.

high tracking frame rate, which requires the use of short TRs. An optimal balance was found to be 5° for a TR of 8 ms. After this nonselective RF pulse, a gradient echo is obtained by applying a readout gradient along one axis.

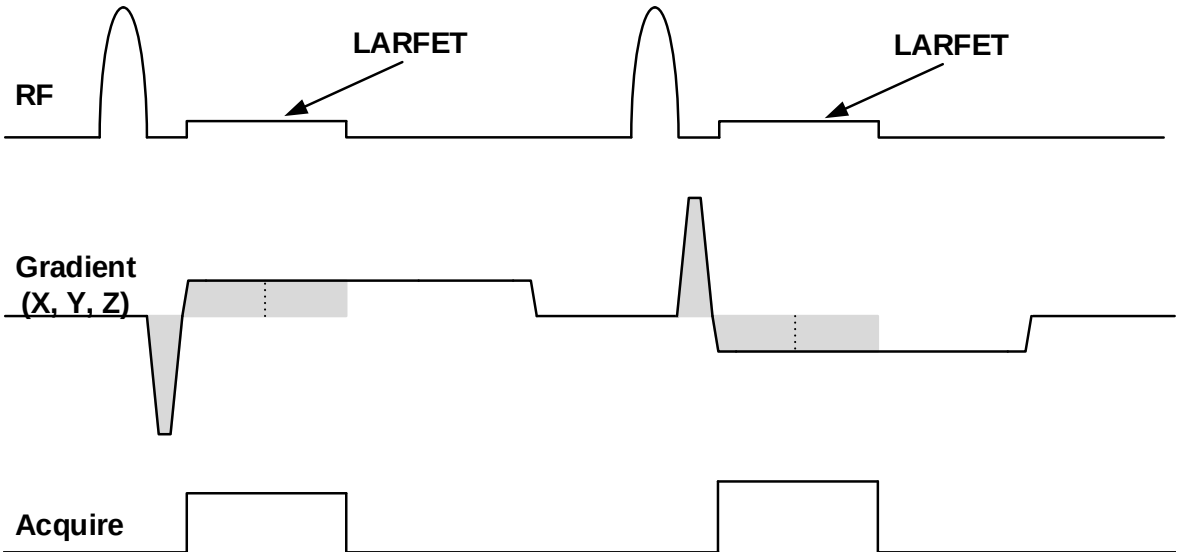

Figure 2.3 The pulse sequence used to localize the coil. A frequency encoding gradient is applied in the direction of localization with a preceding rewinder gradient. LARFET is applied as soon as the readout gradient reaches its flattop and signal acquisition starts. The vertical dotted line indicates the time point where the area of the positive polarity gradient equalized the negative part of the gradient and correspondingly the echo time. To overcome the effect of the resonant offset conditions, two echoes are acquired with opposed polarity gradients.

The angular frequency f_0 of the proton magnetic moment vector that is exposed to a magnetic field B_0 is given by

$$f_0 = \frac{\gamma}{2\pi} \cdot B_0 \tag{2.1}$$

where γ is the gyromagnetic ratio whose value for ^{1}H is $2.68{\cdot}10^8$ rad$\cdot$s$^{-1}\cdot$T^{-1} ($\gamma/2\pi \cong 42.58$ MHz/T). If, however, a gradient G is applied in addition to the static magnetic field, the local frequency is modified:

$$f_{MR} \;=\; f_0 + \frac{\gamma}{2\pi} \cdot G \cdot x \tag{2.2}$$

where x is the location of the protons with respect to the isocenter. Since γ, G, and B_0 are all constant, the precession frequency of the spins is a linear function of their position x. Thus, for nonzero G, by measuring f_{MR}, the frequency of the MR signal, the location of the acquisition point can be determined. Therefore, the frequency of the echo signal is a function of the coil's spatial location and the magnitude of the readout gradient; hence, the location information is frequency encoded. The difference between this sequence and the conventional projection-based tracking method (the 'Dumoulin' method) was the inclusion of an extra, low-amplitude RF pulse (LARFET), which was applied by the body coil during signal acquisition. It served as the reference signal for frequency down-conversion. Its frequency was selected as f_0-300 kHz, with a large offset from the isocenter and outside of the field of view for unambiguous localization. The LARFET pulse amplitude was set to 0.3 V (corresponding to 2.6 dBm transmission power and 0.5° flip angle), which was still detectable by the microcoil inside the bore. The advantage of using the low-amplitude and large frequency offset of the LARFET pulse was the minimal perturbation of the MRI spins. Because of the large offset, LARFET did not excite the spins. However, they were subject to Bloch-Siegert shift since an off-resonance RF field was applied [57, 58]. The phase shift of a spin can be calculated using the formula [58]

$$\omega_{BS} = \frac{(\gamma B_1)^2}{2\omega_{RF}} \tag{2.3}$$

where all the frequencies are defined with respect to the rotational frame. Therefore, by putting $\omega_{RF} = -2\pi{\cdot}300$ kHz and $\gamma \mathrm{B}_1 = 0.5°/3$ ms ≈ 2.91 rad/s into Eq. 2.3, one can obtain $\omega_{BS} \approx -2.24 \cdot 10^{-6}$ rad/s or $f_{BS} \approx -3.57 \cdot 10^{-7}$ Hz, which is negligible.

The measurements might be affected by some resonant offset conditions. Magnetic field inhomogeneities and local susceptibility gradients may also introduce similar errors. These errors are corrected by obtaining two echoes with opposite polarity gradients [38]. In this method, the location was the arithmetic mean of the independently

computed locations from the two echoes. This procedure is repeated for each axis. Hence, four acquisitions are necessary for 2D and six for 3D localization.

The duration of the nonselective RF pulse is 0.5 ms, and the signal acquisition (readout) time is 3 ms. The readout gradient is extended to 6 ms to dephase the spins and prepare them for the next projection block; hence, one projection block has an 8 ms duration in total. As a result, the duration of one 3D complete projection block is approximately 50 ms.

2.1.2 Frequency encoding gradients

During the echo, together with LARFET, a frequency encoding (readout) gradient with a bandwidth of 1 kHz/cm is applied. The amplitude of the gradient is determined from the following equation:

$$G = \frac{2\pi \cdot BW}{\gamma} \tag{2.4}$$

For BW=1 kHz/cm, G is 2.349 mT/m. The opposite polarity dephasing gradient pulse applied before the readout was rectangularly shaped with the highest possible slew rate to obtain the shortest echo time and thus the optimal spatial localization.

2.1.3 The distal unit

The block diagram of the distal unit is shown in Figure 2.4. The microcoil has a diameter of 2 mm with an air inductance of 130 nH. It acts as an antenna to collect the MR signal together with the LARFET reference signal. The frequencies carried in the signal are labeled at each node in Figure 2.4. Passive detuning with crossed Schottky diodes (BAS70-04W, Infineon, Neubiberg, Germany) protects the input of the LNA

from large induced voltages in the coil, although the flip angle amplification effect is not completely eliminated.

Figure 2.5 shows the input stage and LNA configuration. The composite signal is then fed into the LNA through a noise-matching network. The LNA consists of two stages: the first in common emitter (CE) configuration for low-noise operation and the second in common emitter−common base (CE−CB) cascade configuration, for its high stability. All stages use RF NPN transistors (BFP540, Infineon, Neubiberg, Germany).

The LNA has a power gain of 56 dB with a noise figure of 0.9 dB at 123.2 MHz, the center frequency of the scanner. The amplifier was characterized also by measuring the s-parameters with a network analyzer (Rohde&Schwarz ZNC, Munich, Germany) as shown in Figure 2.6. The input impedance is not 50 Ω, since the first stage of the amplifier was biased for lowest NF, rather than maximum power transfer. The measured output impedance is close to 50 Ω, which is the input impedance of the mixer.

The mixer is a Gilbert cell (HFA3101, Intersil, Milpitas, CA, USA). The output of the LNA is connected to both inputs in order to square the signal. Self-mixing is known to be a problem occurring in direct conversion receivers when the strong local oscillator signal leaks into the other input of the mixer. When the DC offset at the mixer output is large, it might saturate the mixer and corrupt the signal. In the current application, self-mixing was not an issue since it was deliberately used to extract the necessary signal $f_{MR}-f_{LA}$ from the two-tone input.

Mixer output is further amplified and band-pass filtered (f_{C1}=10 kHz, f_{C2}=1 MHz, and $A_V\cong$1000) to separate out the component at $f_{MR}-f_{LA}$. Because of the high amplification in this stage, the signal is saturated and a square wave is obtained at the output, suitable for optical transmission. The signal is converted into optical signal by the HFBR-1528 (Avago Technologies, San Jose, CA, USA) and transmitted to the external unit outside the scanner room.

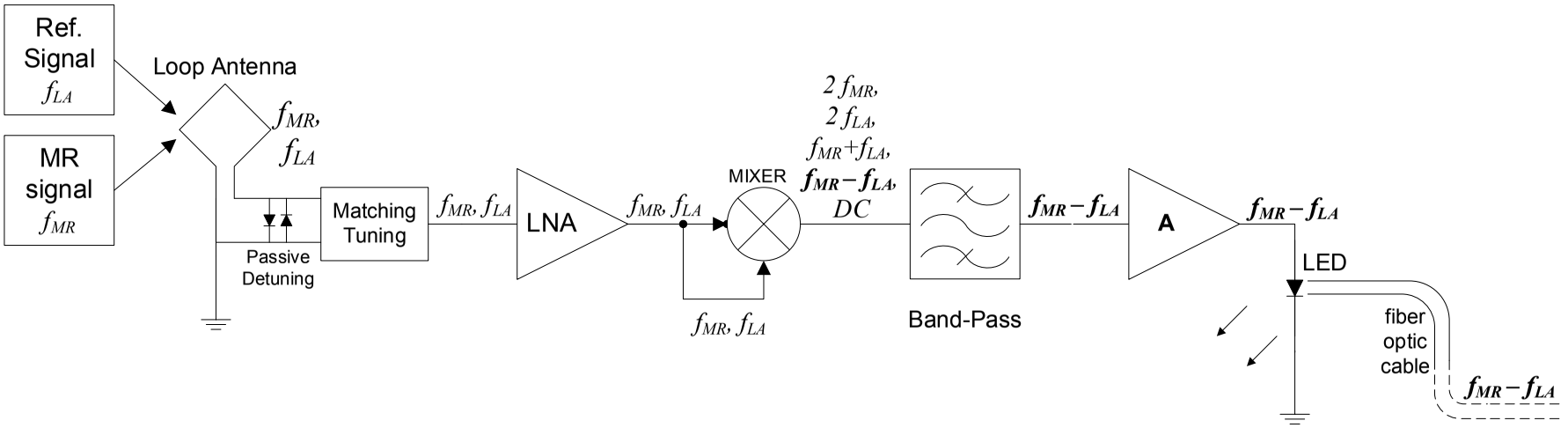

Figure 2.4 The block diagram of the distal unit. Two signals are acquired by the loop antenna (tip coil). f_{MR} is the frequency of the MR signal acquired, and f_{LA} is the frequency of LARFET applied concurrently. After amplification, the signal is multiplied by itself, and at the output of the mixer, combinations of initial frequencies are generated. Among them, $f_{MR}-f_{LA}$ is the location information carrying lower frequency signal. It is extracted by the band-pass filter. The amplifier at the last stage converts the signal into square waves and drives the LED.

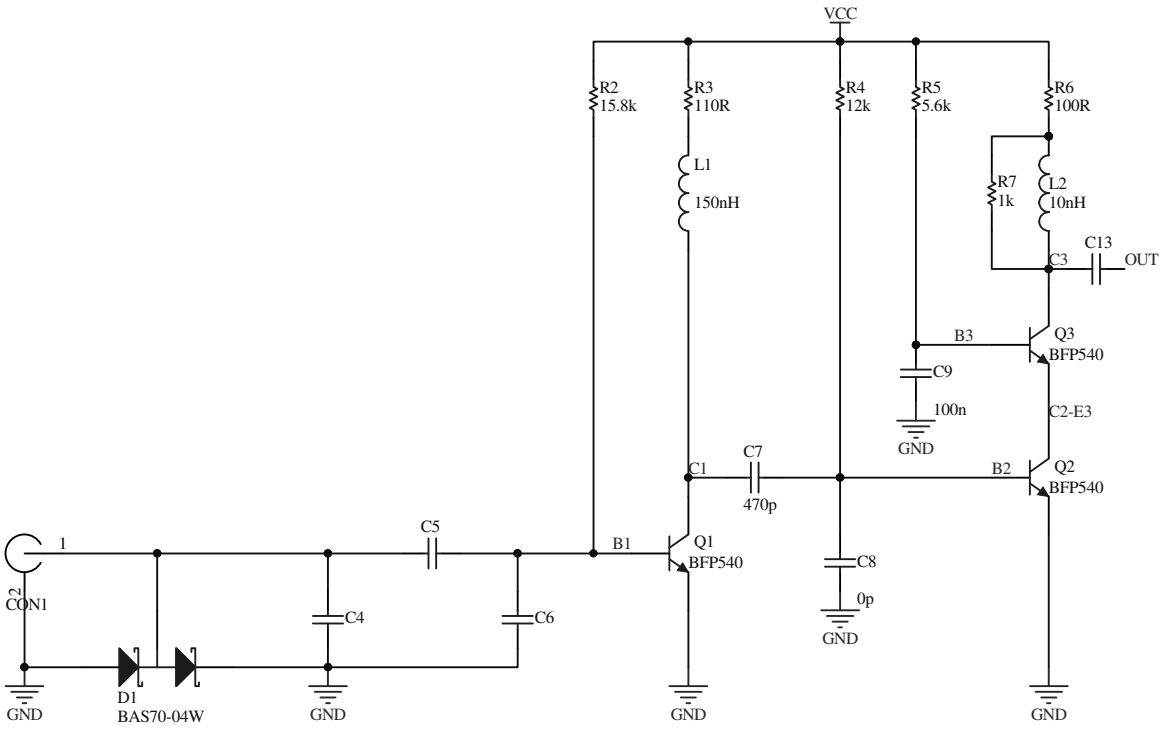

Figure 2.5 The input stage and the LNA. The antenna is connected to C1. Antiparallel pair of Schottky diodes protect the input of the LNA from induced large voltages. The LNA consisted of two stages. The capacitors (or inductors) in Π network were used to bring the antenna impedance to 50 Ω, since the first stage of the LNA was biased such that lowest NF occurred at this value.

2.1.4 The external unit

Figure 2.7 shows the block diagram of the external unit. The signal is reconverted into electrical form using an optical receiver HFBR-2528, which is the counterpart of the HFBR-1528, and finally captured using a digital oscilloscope (DPO4034B, Tektronix, Beaverton, USA). The frequency analysis is performed offline on a PC using Matlab (Mathworks, Natick, MA, USA).

2.1.5 Frequency analysis

Amplification of the weak MR signal at the catheter tip and down-conversion before transmission were crucial for the minimization of losses and ease of transmis-

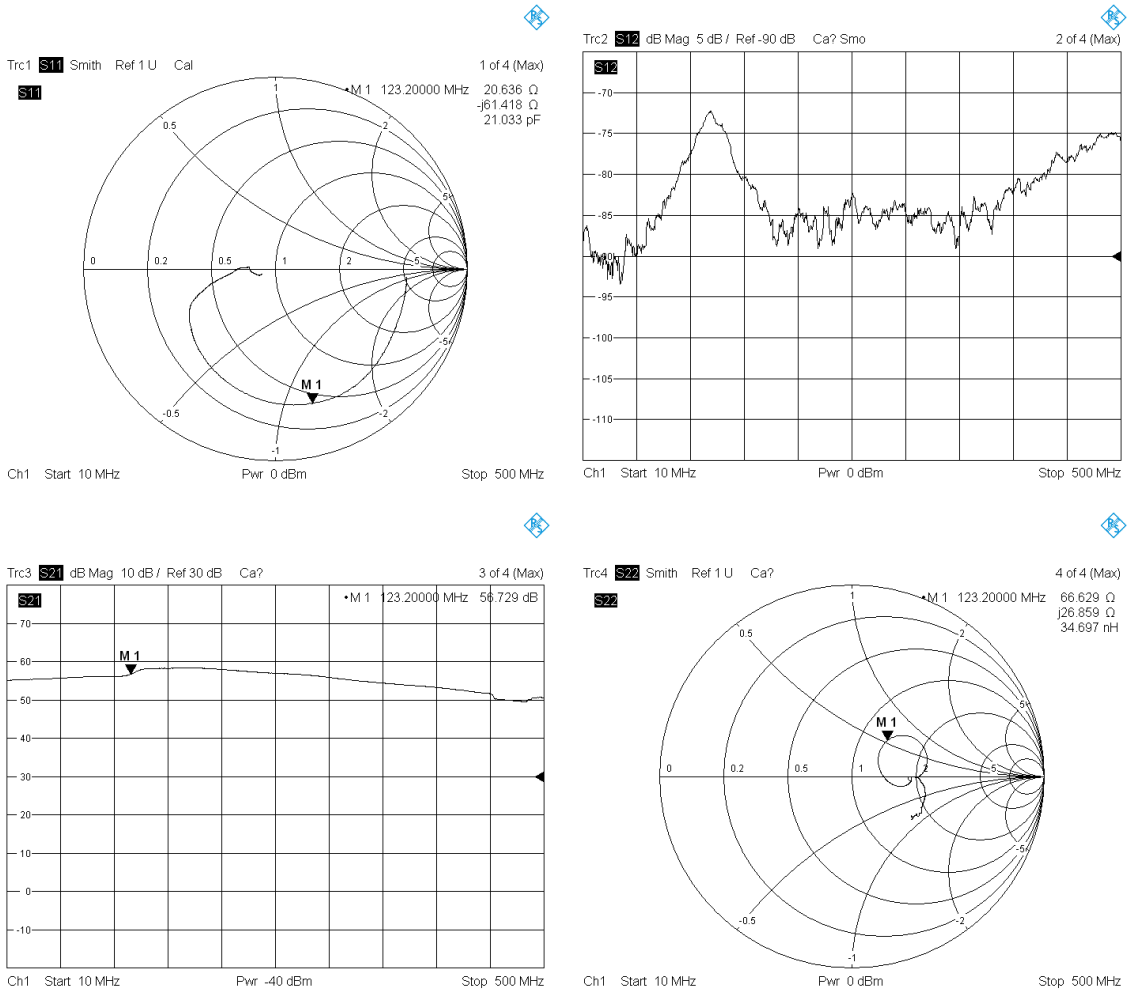

Figure 2.6 The s-parameters of the LNA. The very low value of the reverse transmission coefficient s_{12} gives that there is negligible effect of the output signal on the input port.

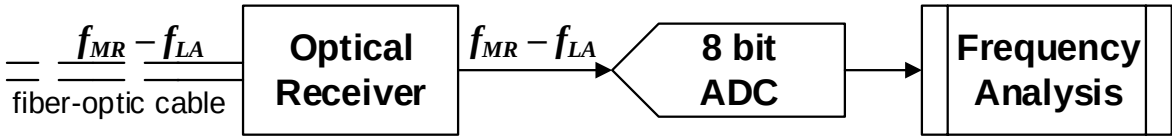

Figure 2.7 The block diagram of the external unit. The frequency of the signal is the down-converted $f_{MR} - f_{LA}$ like at the output of the distal unit.

sion. In our case, the down-converting signal was the LARFET that is simultaneously acquired with the frequency encoded MR signal. As shown in Figure 2.4, $f_{MR} - f_{LA}$ was carrying the frequency encoded location information and separated out here for

analysis.

The frequency analysis consisted of discrete Fourier transform of the discrete time signal. Then the peak in the frequency spectrum was localized, and the position of the coil was computed with the bandwidth (gradient amplitude) taken into account.

f_{LA} in this study was $f_0 - 300\,\text{kHz}$. Combining $f_{\text{Peak}} = f_{MR} - f_{LA}$ with Eq. 2.2, the following was obtained:

$$\begin{aligned} f_{\text{Peak}} + f_0 - 300\,\text{kHz} &= f_0 + \frac{\gamma}{2\pi} \cdot G \cdot x \\ f_{\text{Peak}} - 300\,\text{kHz} &= \frac{\gamma}{2\pi} \cdot G \cdot x \end{aligned}$$

where f_{Peak} is the frequency of the down-converted signal. f_0 was the frequency at the isocenter where $B = B_0$. The exact value of f_0 could differ from the specification provided by the scanner manufacturer. But experimental measurement of it was unnecessary since f_0 was canceled out from the above equation. The above equation also shows the linear relation between f_{Peak} and x. It can be rewritten for x for position calculation:

$$(f_{\text{Peak}} - 300\,\text{kHz}) \cdot \frac{2\pi}{\gamma \cdot G} = x \tag{2.5}$$

where $2\pi/\gamma G$ is $1/BW$, the reciprocal of the bandwidth of the gradient (Eq. 2.4). Defined as $\Delta f/\Delta x$, it gives the change in frequency of the received signal with respect to change in spatial distance from the isocenter as discussed in section 2.1.2. As a result, the microcoil location was calculated using the formula

$$\text{Location} = \frac{f_{\text{Peak}} - 300\,\text{kHz}}{BW} \tag{2.6}$$

To determine the peak frequency more precisely, the data was lengthened in the time domain using zero padding, resulting in higher resolution in the frequency spectrum. Zero padding to a power-of-two length also contributed to faster execution of FFT, the popular DFT algorithm. Taking the Fourier transform of a signal of length N_0 after zero padding and lengthening it to N_1 means N_1/N_0 times denser sampling of the DTFT which is continuous in frequency domain.

2.2 Results

The concept verification experiment was conducted at 27 different positions in a 3×3×3 grid as shown in Figure 2.1.

Figure 2.8 shows the frequency spectrum of a sample signal acquired from an off-center position. The spectrum is normalized to its peak value whose location on the frequency axis was used to determine the physical location of the coil experimentally. For every position in the grid, six similar graphs were obtained, namely, for all three axes and both gradient polarities. For each axis, the physical coordinate is considered to be the arithmetical mean of the independently computed locations from opposite polarity gradient signals.

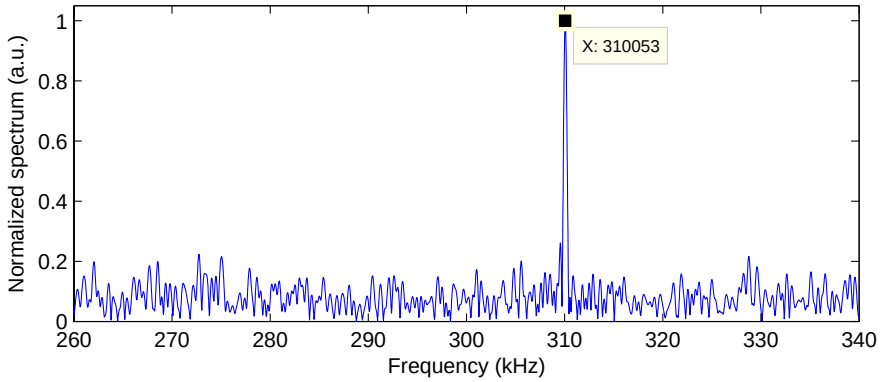

Figure 2.8 A sample frequency spectrum obtained during the experiment. It has a sharp peak at 310053 Hz corresponding to a location 100.5 mm off-center. The last digit can be ignored because it is below the precision of the system.

In Figure 2.9, the nine MR images acquired for holes 31 to 39 were added up and shown as one image. The computed locations were superimposed as a green plus

sign for comparison. A good visual correlation was observed. Similar images can be obtained for any coplanar nine holes in the 3D grid.

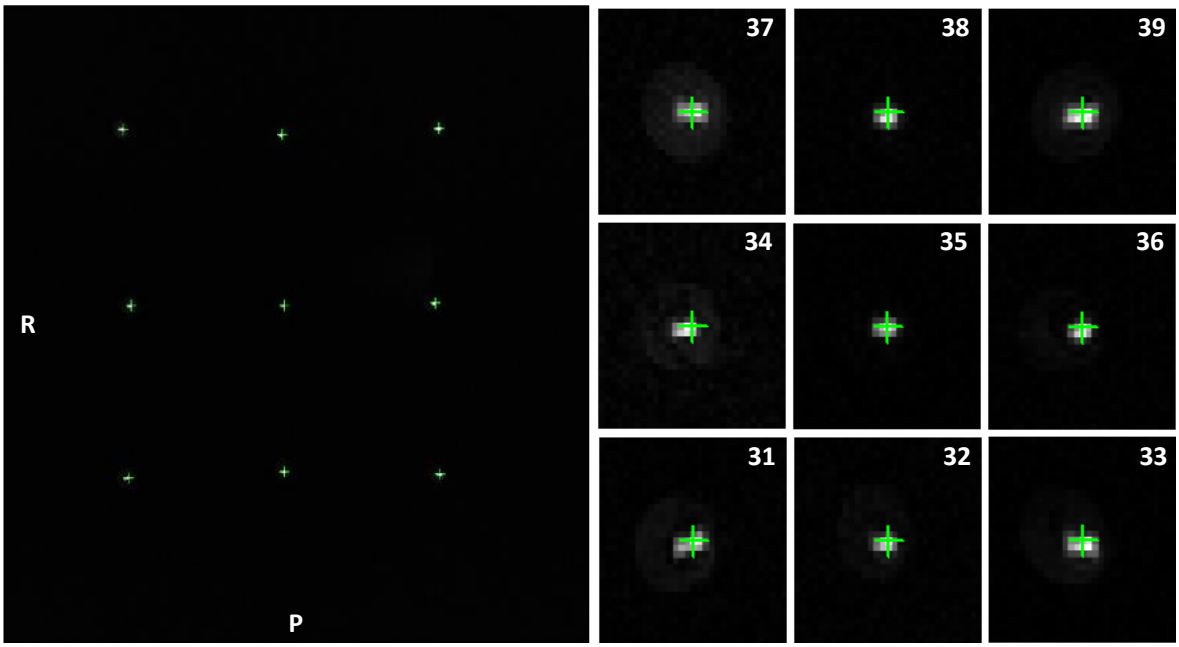

Figure 2.9 **Left:** The nine transversal MR images acquired for locations 31 to 39 are added up and shown as one image. The computed locations are also superimposed as green plus signs. **Right:** Zoomed images for better visualization.

For numerical comparison, a second set of locations was extracted from the images by segmenting the bright spot regions and determining their centers as shown in Figure 2.10. For a more precise localization, interpolation was performed within the region of interest containing the bright spot.

The graphs in Figure 2.11 show the errors of the proposed system with the exact locations assumed to be the bright spot centers on the MR images. They are all $\leq$0.8 mm.

2.3 Discussion

There was a significant match with the bright spot region on the MR images and the experimentally determined locations. A numerical comparison showed that

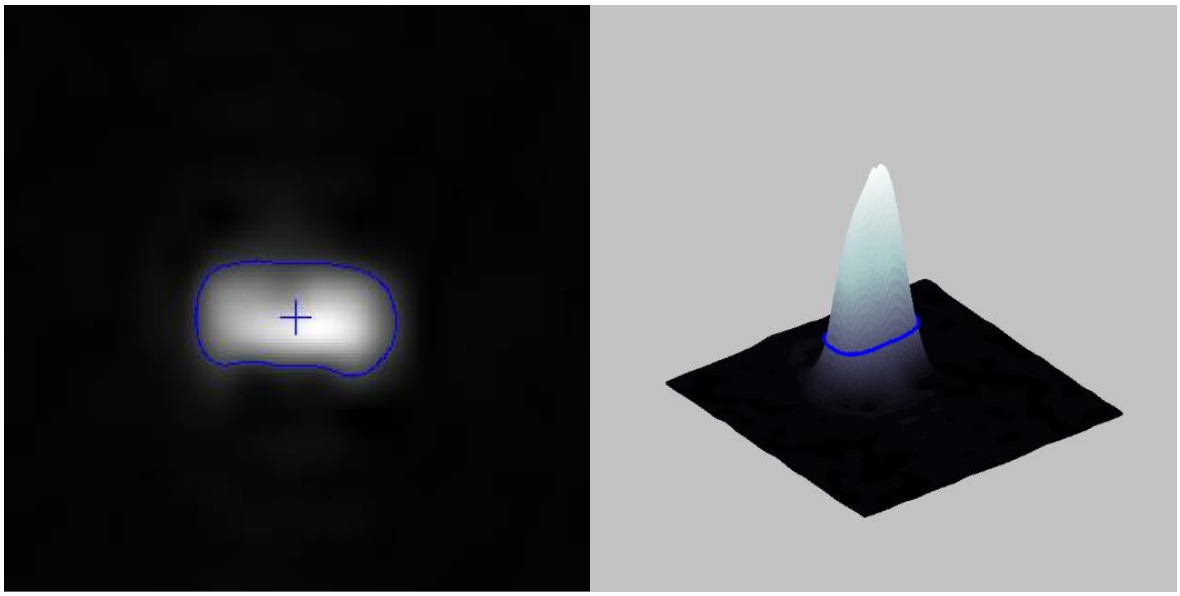

Figure 2.10 Left: Determination of the center of a sample bright spot. The center is designated with a plus sign. Interpolation is used for subpixel localization. **Right:** 3D plot of the region of interest. It shows the bright spot as a hill and its boundary as a contour line.

the maximum error of the system was around 0.8 mm, which corresponds to 1 pixel for a 512 × 512 image of 40 cm FoV. This is mainly due to the fact that imaging experiences the same amount of distortion from the magnetic field inhomogeneities, as the proposed method. Taking the physical size of the coil into account ($\varnothing$ = 2 mm, l = 3 mm), an error of 0.8 mm ($\leq$1 pixel) is acceptable. This is also far better than required accuracies for many interventional procedures and comparable to error ranges of similar active tracking systems [59, 60]. Reducing the image resolution within the same FoV can result in a broader spatial coverage of the center pixel, and the location found by the system may fall in it rather than the neighbour pixel, thus virtually increasing the accuracy of image guidance. The accuracy with current configuration can also be improved, when necessary, by repeating the measurements and averaging at the expense of increased localization time. Since this method is highly sensitive to magnetic field inhomogeneities, for procedures like biopsy, where the absolute location would be needed, this method should be applied carefully and only near the isocenter, where the inhomogeneities and consecutively the distortions are smallest.

The precision of the system depends on the spacing in the discrete frequency

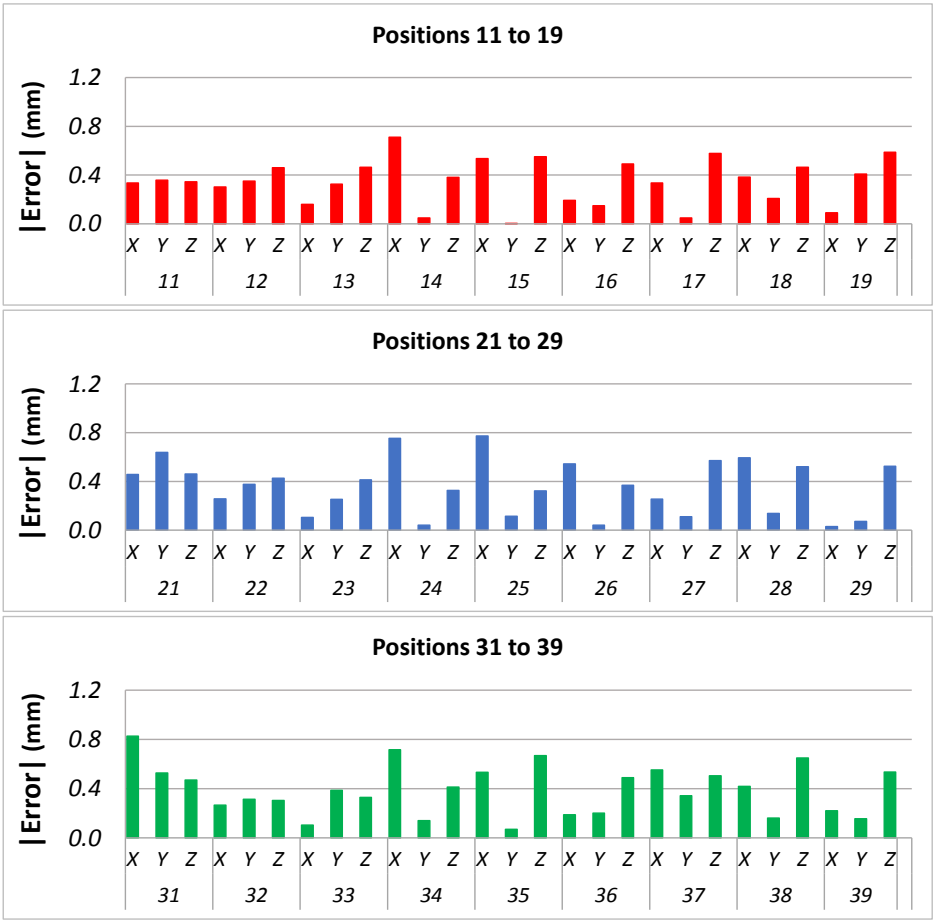

Figure 2.11 Absolute errors calculated from the experimentally determined coordinates and the positions of the coil determined from the MR images. The numbers on the x axes give the hole number.

domain data (Δf), which is the sampling frequency divided by the number of samples:

$$\Delta f = \frac{f_S}{N} = \frac{1}{L}$$

where L is signal recording time. In the formula, it seems possible to reduce the bin spacing in the frequency domain and accordingly to increase the spatial resolution by lengthening the recording time L, namely, looking at more data at the expense of increased localization time. Zero padding, however, as mentioned in section 2.1.5, can increase the data length N without really increasing the recording time. Although it does not improve spectral resolution, which is related to resolving closely spaced features in the frequency domain, it can provide a more precise localization of the peak frequency. Figure 2.12 shows the plots obtained with and without zero padding. With f_S=27.78 MS/s and L=3 ms, 83.3 k data points were obtained per projection. By zero

padding and extending this to 2^{19} (512 k points), a precision of approximately 50 Hz in peak detection and consecutively 0.5 mm in localization could be achieved with no increase in total localization time (TR = 8 ms). This can also be reduced to 32 ms by using Hadamard encoding [38] instead of the 6 excitation scheme.

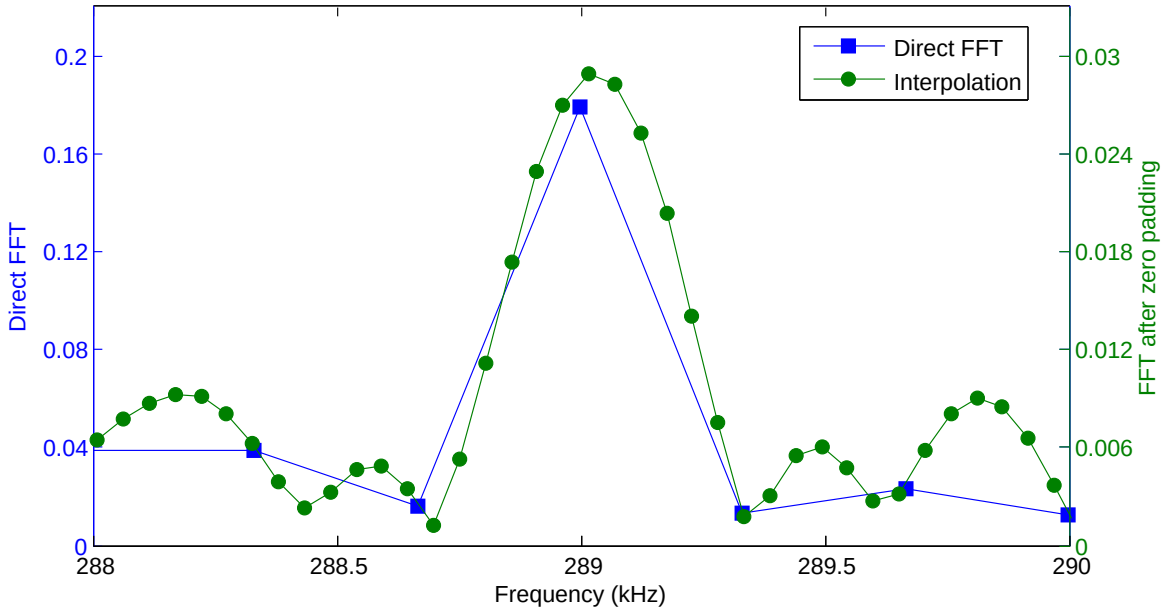

Figure 2.12 Effect of sinc interpolation due to zero padding before Fourier transform. Extending the data length from 83,333 to 524,288 resulted in 6.3 times denser sampling of the DTFT which is continuous in frequency domain and increased localization resolution by the same amount. Note that, the values of the new plot are also attenuated by 6.3. But this did not decrease SNR, because noise in the signal was attenuated, too.

3. The Leaky 125 MHz Signal

In Siemens 3 T scanners, there is an intrinsic 125 MHz signal that is used to modulate a lower frequency signal to obtain the RF pulses around 123.2 MHz. This 125 MHz signal leaks through the RF transmission system and is detectable whenever the RF transmitter is turned on. In this study we propose using this leaking signal for frequency down-conversion of the MR signal as an alternative to the LARFET.

3.1 Characteristics of the leaky 125 MHz signal

The source of the signal is the synthesizer in the RF pulse generator as described in the Siemens patents [61]. The synthesizer serves to output the base frequency, for example of 125 MHz given a ^{1}H excitation in 3 T systems. The modulator converts the digital signal generated by the control computer into an analog RF signal and upmixes it with this base to obtain the desired transmission frequency.

It is a better approach to describe the effect of this signal in terms of transmission power. But there is no simple method to measure it directly. Instead, its power can be measured against RF pulses within the same exposure. Spectrum analyzer measurements with a simple loop antenna showed that unlike RF pulses, its amplitude does not vary with increasing flip angle. When doubling the flip angle, the power ratio of the RF pulse and 125 MHz signal shows an increase of approximately 6 dB as shown in 3.1. This is due to the doubled amplitude of the RF pulse ($20\ log\ 2\ \approx\ 6$). If the amplitude of the 125 MHz signal would double too, the ratio would be the same. It can be concluded that the power of the 125 MHz signal remains the same regardless the flip angle (i.e. amplitude) of the RF pulse. It is always available whenever the transmission system is turned on regardless the amplitude of the RF pulse even with pulses of 0° (0 V amplitude) and has constant amplitude (i.e. rectangular shaped). Since measuring the effect of the 125 MHz signal in terms of transmission power is not

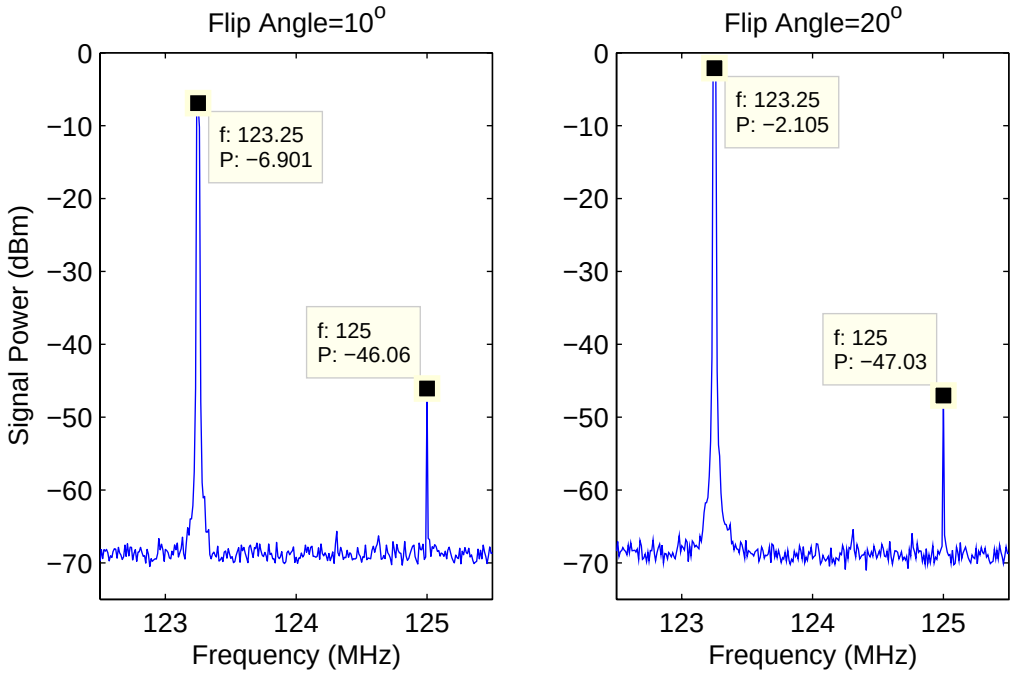

Figure 3.1 Comparison of the powers of RF pulses against the power of the 125 MHz signal measured using a portable spectrum analyzer (Rohde&Schwarz, R&S®FSH4, München, Germany). For a flip angle of 10° the difference is 39.2 dB where it increases by 5.77 dB when doubling the flip angle (i.e. 20°).

straightforward, using a different measure such as flip angle can be more convenient. To do this, the power of the 125 MHz signal was measured against RF pulses with known shapes (i.e. sinc or rectangular) and duration.

Sinc pulses used in MRI are usually apodized using a Hanning window to overcome the ringing effect due to truncation. It is also the case with Siemens systems. The apodized envelope sinc pulse is defined as:

$$E(t_i) = 0.5 \cdot \left(1 - \cos\left(2\pi \cdot \frac{t_i}{T}\right)\right) \cdot \mathrm{sinc}\left(\pi \cdot \frac{BWT}{T} \cdot t_i\right) \tag{3.1}$$

where T is the pulse duration and BWT is the bandwidth time product. Then its power can be calculated as:

$$P_{sinc} = \int_{-T/2}^{T/2} \left[k \cdot E(t_i) \cdot \cos(\omega t)\right]^2 dt \tag{3.2}$$

where ω is the frequency of the RF pulse (f=123.2 MHz for the Siemens Trio system), k is the multiplier determined by the scanner to adjust the flip angle. The flip angle is however simply the integral of the envelope:

$$P_{sinc} = \int_{-T/2}^{T/2} \left|k \cdot E(t_i)\right| dt \tag{3.3}$$

For the sinc pulse with T=1 ms and BWT=2.70 used in the measurement, the power and flip angle are calculated as $5.33{\cdot}10^{-5}k^2$ and $1.678{\cdot}10^{-4}k$ respectively.

The power of the leaking 125 MHz signal can be calculated as:

$$P_{125} = \int_{-T/2}^{T/2} \left[A \cdot \cos(2\pi \cdot 125\ \text{MHz} \cdot t)\right]^2 dt = 5 \cdot 10^{-4} A^2 \tag{3.4}$$

where A is the amplitude of the leaking 125 MHz signal. The flip angle is simply $10^{-3}A$ for this rectangular pulse.

In the case with FA_{sinc}=20°, the ratio of the RF pulse power and leaking signal is:

$$\frac{P_{sinc}}{P_{125}} = \frac{5.33 \cdot 10^{-5} k^2}{5 \cdot 10^{-4} A^2} \cong 44.93\ \text{dB} \Longrightarrow \frac{k}{A} \cong 540.3 \tag{3.5}$$

Using this ratio in the flip angle ratio equation gives the flip angle of the leaky signal:

$$\frac{FA_{sinc}}{FA_{125}} = \frac{1.678 \cdot 10^{-4}}{10^{-3}} \cdot \frac{k}{A} \Longrightarrow FA_{125} \cong 0.221^{\circ} \tag{3.6}$$

A similar calculation for the case with $FA_{sinc} = 10^{\circ}$ resulted in $FA_{125} \approx 0.214^{\circ}$. Using these results, it can be concluded that the flip angle effect of the leaking 125 MHz signal is around 0.2°. This definition may be confusing, since the frequency 125 MHz is outside the excitation bandwidth and therefore this leaky signal has no effect on the spins (except the negligible Bloch-Siegert effect). But the flip angle is a meaningful measure when comparing this signal to LARFET.

3.2 Materials and Methods

To demonstrate the usability of the intrinsic 125 MHz signal for device localization, the experiment with the LARFET method was repeated with the LARFET amplitude set to 0 V (0° flip angle). For each of the twenty-seven positions as seen in Figure 2.1, first an image was acquired, where the location of the coil is visible as a bright spot due to local flip angle amplification effect. Then, the location was experimentally determined and compared to the location of the brightest pixel in the MR image.

3.2.1 Positional localization pulse sequence

Figure 3.2 shows the pulse sequence, starting with a non-selective RF pulse to excite all the spins. Then a gradient echo was obtained by applying a readout gradient on one axis. As explained in the theory part, depending on the magnitude of the gradient, the frequency of the echo signal acquired by the microcoil is a function of

its spatial location. But the measurement could be affected by some resonant offset conditions. Magnetic field inhomogeneities and local susceptibility gradients may also introduce similar errors. These errors were corrected by obtaining two echoes with opposite polarity gradients; the location is the arithmetic mean of the independently computed locations from the two echoes [38]. This procedure was repeated for the remaining two axes. So, 6 acquisitions were necessary for 3D localization.

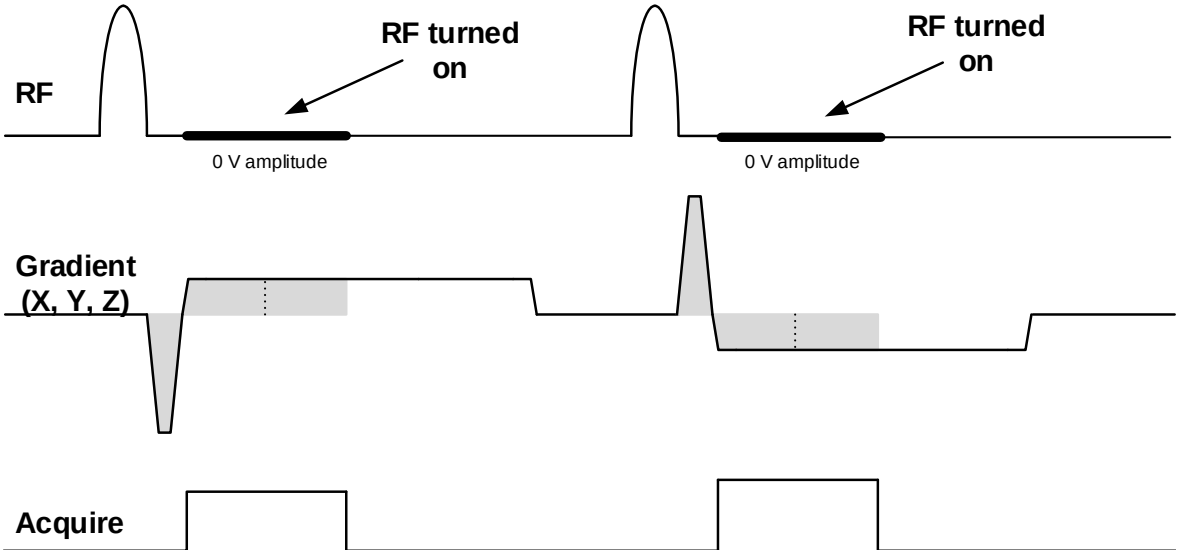

Figure 3.2 The pulse sequence used to localize the coil.

3.2.2 The distal unit

For this experiment the same distal unit as in LARFET method was used. But since the center frequency was 1.8 MHz instead of 300 kHz, the BPF was modified to f_c=1.8 MHz, BW =1 MHz, A_V=1000 to separate the component at 125 MHz$-f_{MR}$. Due to the high amplification in this stage, the signal is saturated and a square-wave is obtained at the output, suitable for optical transmission.

3.2.3 Frequency analysis

The frequency analysis consisted of Fast Fourier Transform (FFT). The peak in the frequency spectrum corresponded to the physical location of the coil within the scanner. In our previous work, zero padding before FFT was employed for two reasons: First, to bring the discrete data to a power-of-two length for the FFT to run efficiently. And second, to achieve closer bin spacing in the discrete frequency spectrum for more precise peak localization. Zero padding in time domain corresponds to convolution with a sinc function in frequency domain and thus a denser sampling in the frequency domain. In this work, zero padding was used to bring the data to the nearest power-of-two length for efficient FFT calculation instead. After that, sinc interpolation was separately applied and only near the peak region. This is supposed to reduce the total calculation and consecutively the localization time.

3.3 Results

The concept verification experiment was conducted for twenty-seven different positions as was shown in Figure 2.1. To find the location, the deviation of the peak in the frequency spectrum from 125 MHz$-f_c$ is used. It is around 1.8 MHz for Siemens 3 T scanners. Figure 3.3 shows the frequency spectrum of a sample acquisition and the peak obtained from sinc interpolation.

The real value of f_c may differ from the given one in the scanners specification. Luckily, there is no need to measure it experimentally or read it directly from the console. The frequency of the difference signal is:

$$f_{x\pm} = 125\text{MHz} - f_c \mp BW \cdot x \tag{3.7}$$

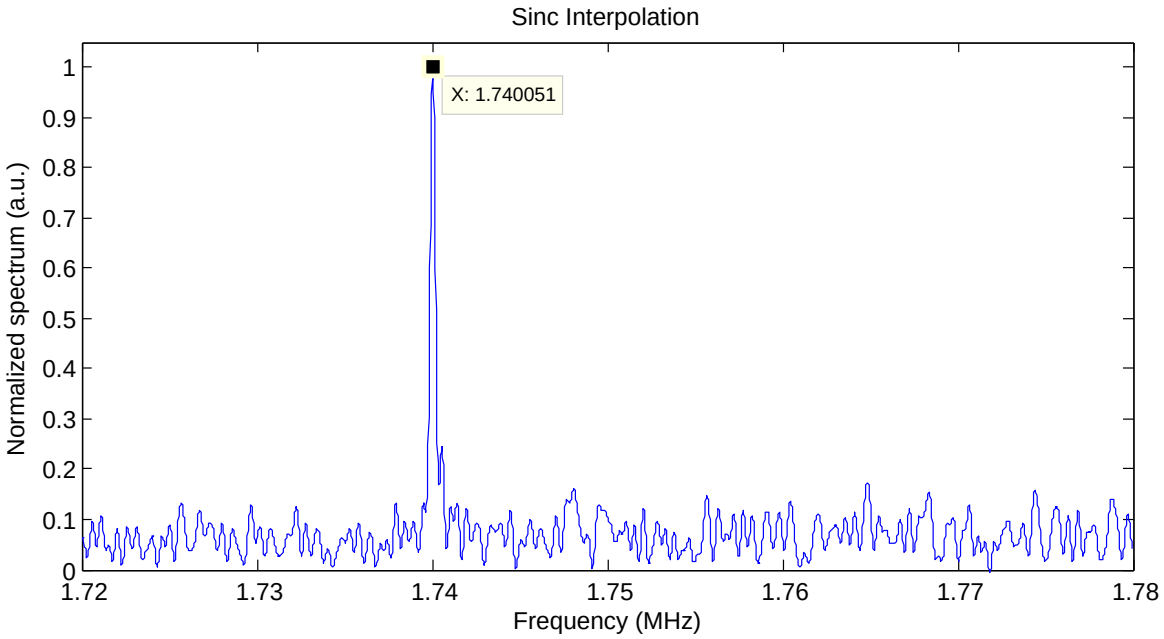

Figure 3.3 The frequency spectrum of a sample acquisition. The peak was obtained by zooming the region around 1.75 MHz region which is approximately 125 MHz$-f_c$ and applying sinc interpolation.

where the offset from f_C depends on the position and polarity of the gradient. For the opposite sign gradient the terms 125 MHz and f_c cancel out, simplifying the calculation to:

$$x = \frac{f_{x+} - f_{x-}}{2 \cdot BW} \tag{3.8}$$

MR images with the computed location superimposed as a green plus sign for a better visualization and easier comparison are shown in Figure 3.4. Good visual correlation between the computed locations and actual locations on images can be seen.

The experimentally determined locations matched the locations found on the images mostly within the range ± 0.8 mm which corresponds to 1 pixel for a 512x512

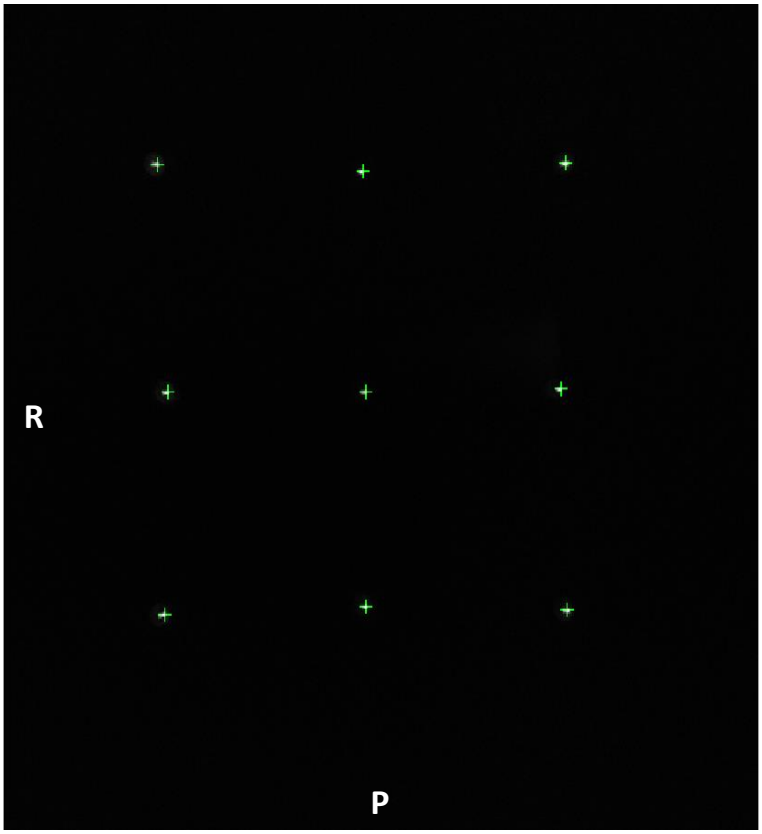

Figure 3.4 For each experiment the computed location is superimposed as a green plus sign on the acquired MR image. The center of the plus sign matches the brightest point that corresponds to the actual location within one pixel.

image of 40 cm FoV. Only for a few points the error increased to 1.2 mm (Figure 3.5). Taking the physical dimensions of the coil ($\varnothing$ = 2 mm, l = 3 mm) into account, it is below the tolerable error range.

3.4 Discussion

The 125 MHz leaky signal has a constant amplitude, which corresponds to 0.2° flip angle. Due to its weakness, the down-converted signal and consequently SNR of the localization signal dropped for some measurement points. However, the location calculations did not suffer from lowered SNR, because it was still high enough to detect the peak.

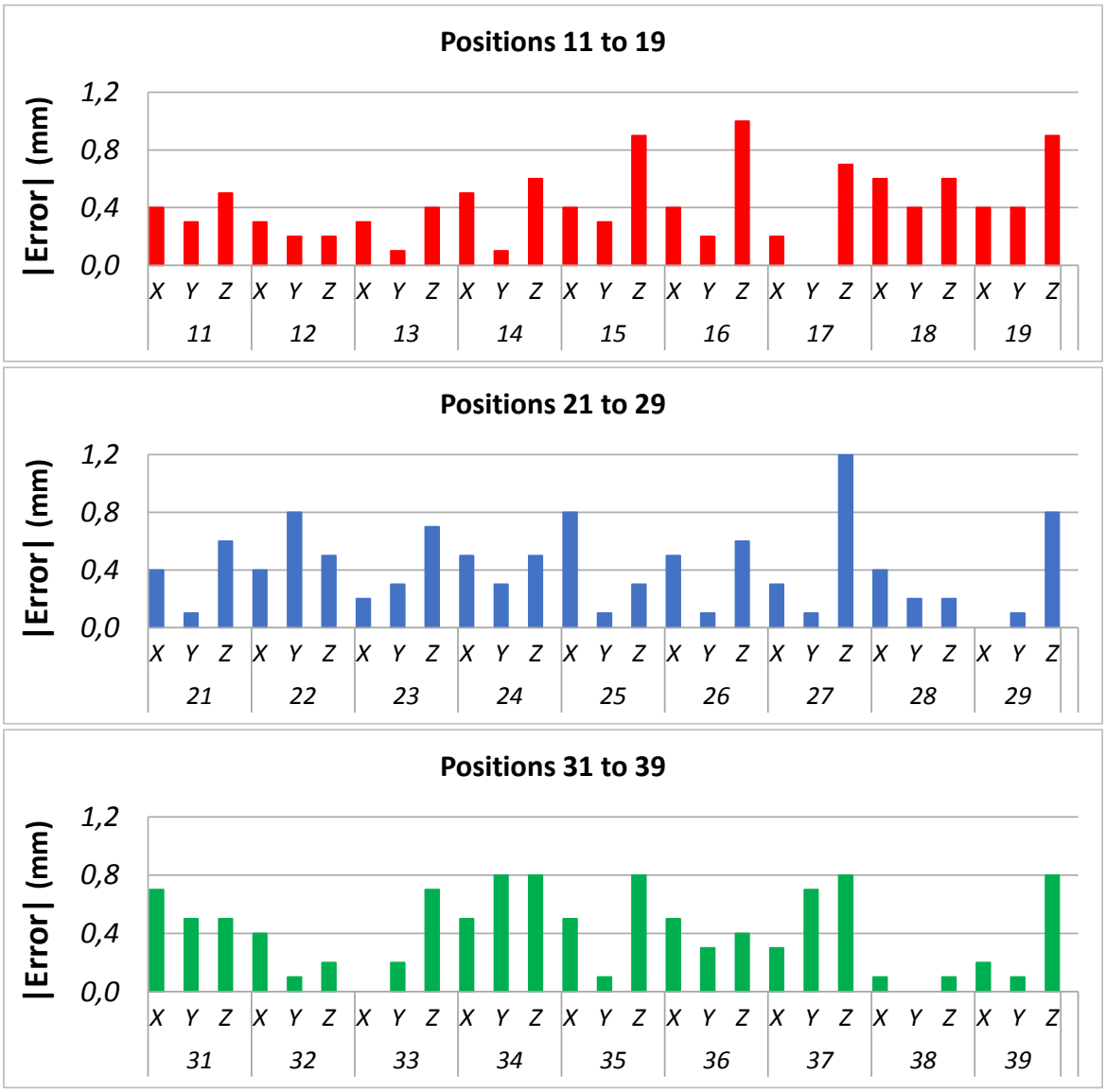

Figure 3.5 Errors between the locations calculated from the images and experimentally determined locations. Most of them are subpixel.

The leaky 125 MHz signal is available only on Siemens 3 T scanners. Siemens 1.5 T scanners have a similar signal at 65 MHz (f_C=63.6 MHz) as shown on Figure 3.6. This is due to the structure of the RF transmission system. Since it is patented to Siemens [62], this method seems not feasible on scanners of other manufacturers.

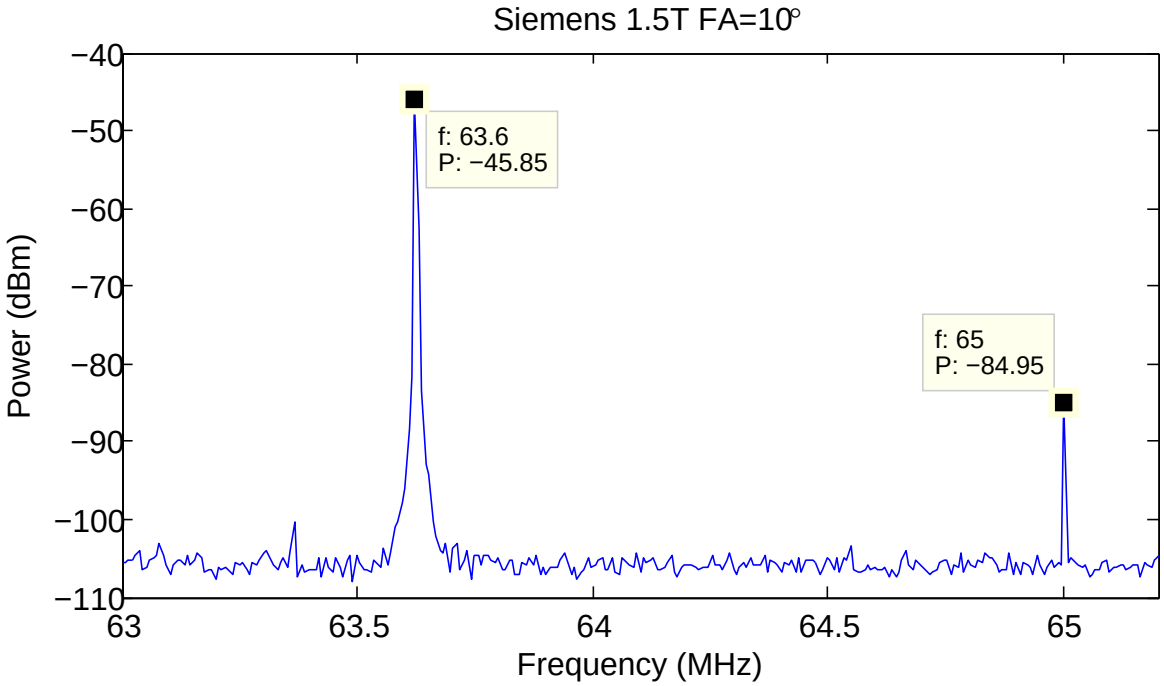

Figure 3.6 Plotted measurement data of the spectrum analyzer connected to a loop antenna placed inside the bore. The peak at 63.6 MHz corresponding to the RF pulse was accompanied with another peak at 65 MHz.

4. Attempt to Miniaturize the System

To show that this system could be miniaturized, an ultra low power CMOS-based optoelectronic was implemented in a standard 0.18 μm UMC CMOS triple-well technology [63]. The system architecture is shown in Figure 4.1. The microcoil is externally connected similar to PCB versions. The block receiver consists of an differential LNA and a differential mixer in Gilbert-Cell configuration. An op-amp with a large gain at the output of the mixer amplifies the low-frequency output signal and feeds it into a comparator which converts the signal into square pulses and drives the laser diode which is the electro-optical signal convertor.

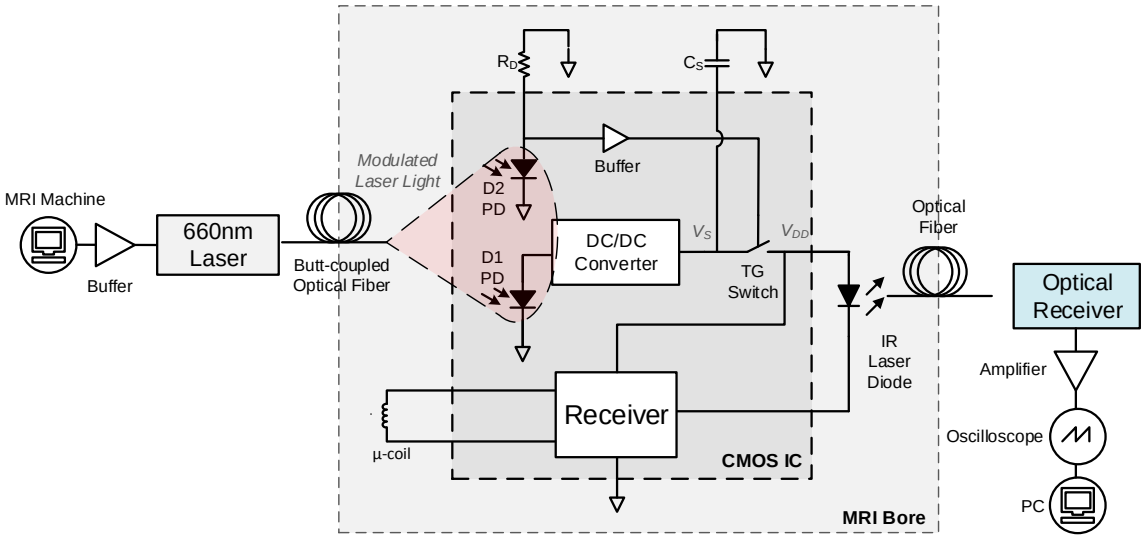

Figure 4.1 The block diagram of the miniaturized system.

Since no long conducting cables are allowed in MR environment, the power to the circuitry is delivered also optically from a 660 nm laser source and via an optical fiber. The laser source is synchronized with the scanner such that it delivers power during time intervals between successive localizations. The laser falls on two on-chip photodiodes D1 and D2. The voltage generated across the terminals of D1 under incident light is 0.55 V. The DC-DC converter boosts this voltage up to 1.6 V, which is sufficient for the electronics to function, and charges a large capacitor C_S at the output. D2 drives a switch between the output of the charge booster and the receiver circuitry.

As the localization starts the external laser source is turned off and the switch is closed connecting the capacitor which was charged to 1.6 V to the receiver to power it up.

Heating of the microsystem, due to laser illumination is experimentally characterized by monitoring the temperature of the die using a Fisher Scientific 06-664-39 traceable noncontact infrared thermometer. Average of 15 steady state measurements were recorded for each laser power level. Temperature difference due to laser illumination for 50 mW and 60 mW of optical power levels are 1°C and 2°C, respectively.

Figure 4.2 shows the micrograph of the IC and the PCB used to connect the peripherals to it. As can be seen from the figure, among the components of the IC, D1 has the largest area to produce large enough current for charging C_S. D2 has a small area and consecutively small leakage capacitance allowing fast switching when localization starts and ends. The IC was encased in an IC package with the top side left open for optical fiber coupling. The antenna was connected to the circuitry via an SMA connector as in previous experiments. The output LED was selected from infrared range because of its low V_f 1.2 V. The optical fiber from the laser source was inserted into a plexiglass holder for IC coupling to avoid any misalignment of the fiber with the photodiodes during operation.

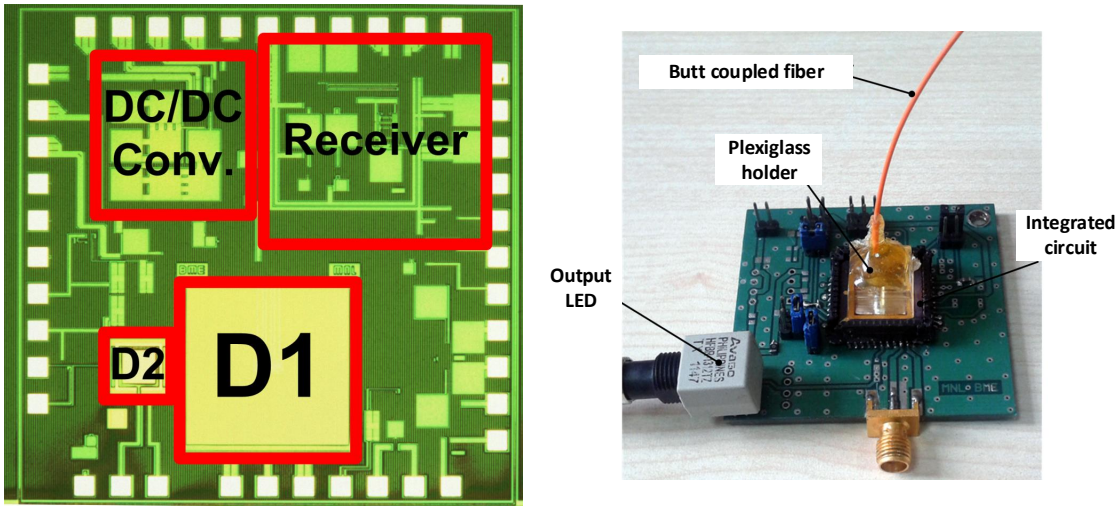

Figure 4.2 **Left:** The micrograph of the IC. **Right:** The whole system for the experiment.

4.1 Experiment

The system was tested in four different locations along the x-direction (i.e. right-to-left) using LARFET method. The synchronization signal from the scanner was used as the modulation signal for the laser source. Localization period and acquisition time were set to 40 ms and 1 ms, respectively. The bandwidth of signal was set to 3 kHz/cm to compensate for the reduced acquisition time. The laser light was delivered to the IC through a 6 m long, multi-mode optical fiber with a core diameter of 62.5 μm. The light output of the IC was connected to an external optical receiver via a similar cable. Output of this optical receiver was amplified by a voltage amplifier (Stanford Research Systems-SR445A, 56 dB gain) and captured by an oscilloscope (Agilent DSO6104A) for frequency analysis.

4.2 Results

The frequency spectra of the signals acquired from these four locations are given in Figure 4.3 and Figure 4.4 using the LARFET and the 125 MHz leaky signal as reference signal, respectively. In this experiment the total signal acquisition time was reduced to 1 ms Signals from off-center locations have remarkably low SNR. Another reason for the low SNR is the higher bandwidth (i.e. larger gradient amplitude), because there exists a relationship $SNR \propto 1/\sqrt{G}$ between SNR and the gradient [64]. However, the peaks are still clearly distinguishable from the noise floor. The peak frequencies and corresponding locations are given in Table 4.1 and 4.2.

Table 4.1
The results of the experiments with the IC using LARFET as the reference signal.

	Position1	Position2	Position3	Position3
Peak frequency (kHz)	263.60	282.67	299.17	347.90
Computed location (mm)	−121.3	−57.8	−2.8	159.7

Table 4.2
The results of the experiments with the IC using the leaky 125 MHz signal as reference. The experimentally determined locations differ in 1.5 mm for LARFET and 125 MHz leaky signal.

	Position1	Position2	Position3	Position3
Peak frequency (kHz)	1787.38	1768.30	1752.66	1703.07
Computed location (mm)	−122.6	−59.0	−6.87	158.4

4.3 Discussion

A fully optical, CMOS-based active device localization system was designed and implemented. The system was powered from an optical power supply. Hence, conducting cables susceptible to RF heating during RF transmission were completely eliminated. The proposed system was tested in MRI environment and its localization capability was successfully demonstrated. The power supply capacitor C_S could supply the active part only for 1 ms before its voltage dropped below 1.2 V, the safe limit for the operation. This would cause a decrease in the resolution of the frequency domain data, consecutively in spatial localization of the microcoil according to Eq. 2.6 and Eq. 3.8. To compensate for the reduced signal acquisition time, the bandwidth (i.e. gradient amplitude) was tripled and set to 3 kHz/cm.

In its current form, the system requires two fiber optical cables connected, one for power delivery and one for signal transmission, complicating the mounting process to the tip of a catheter for clinical use. In future, using a single optical fiber for both powering and optical signal transmission may be considered.

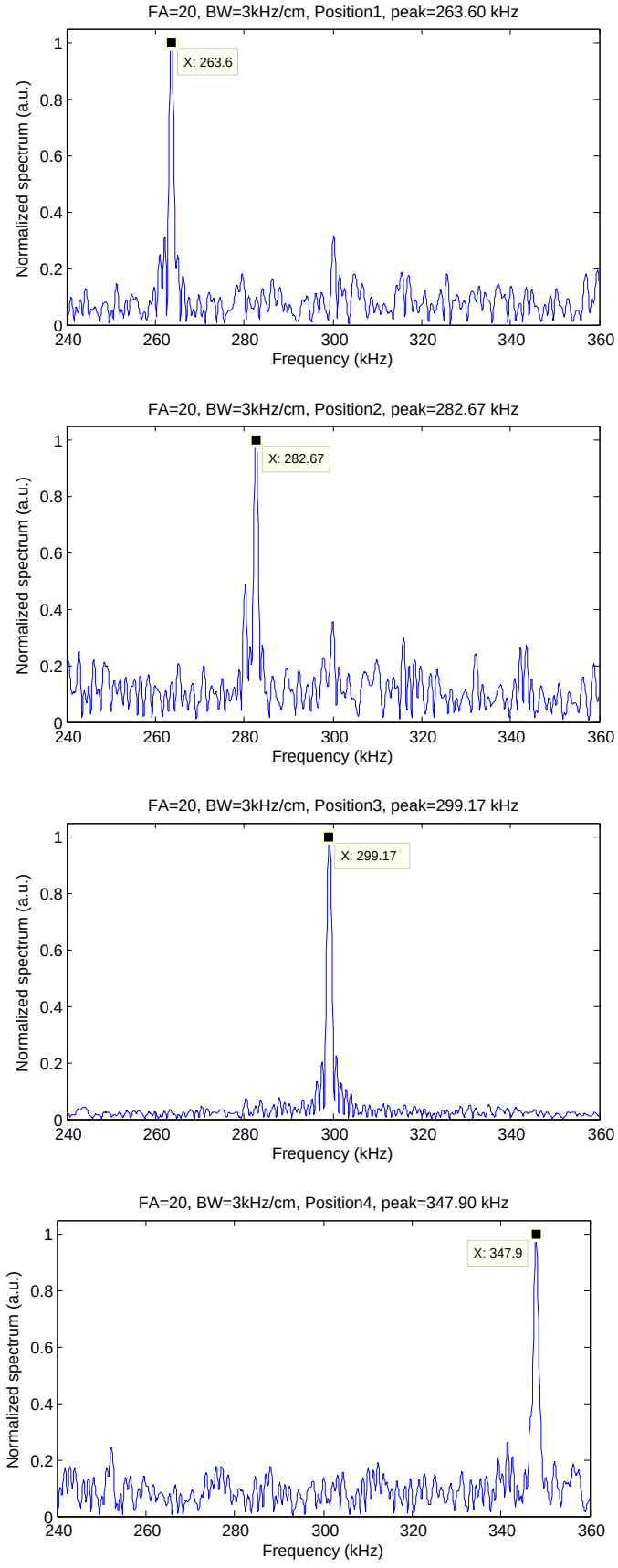

Figure 4.3 The FFT plots of the signals captured at four different locations using the LARFET method.

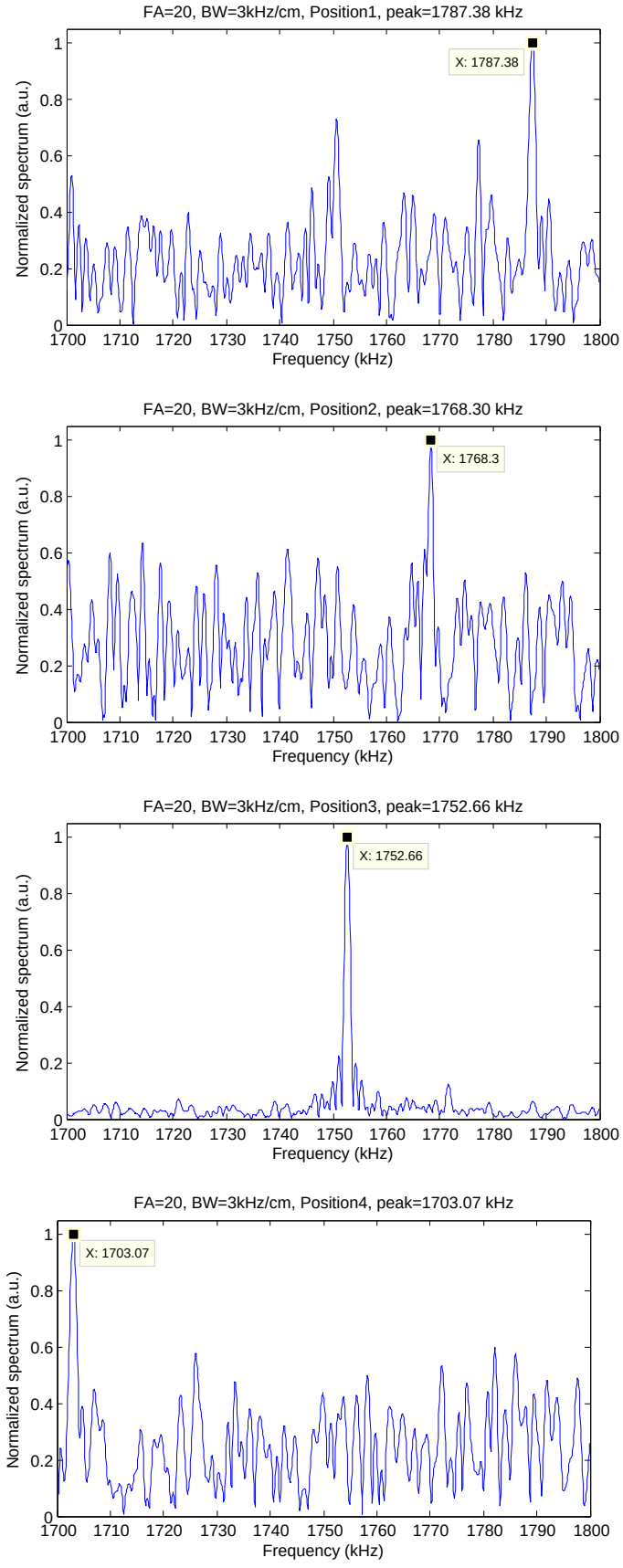

Figure 4.4 The FFT plots of the signals captured at four different locations using the 125 MHz leaky signal as reference. Signals from off-center locations have remarkably low SNR.

5. Conclusion

A low-amplitude RF pulse was successfully used as a precisely tuned down-converting signal in MRI device localization. Since the location information is encoded in frequency, the accuracy of the localization is dependent on the frequency accuracy of the down-converting signal. In this case, it is as reliable as the MR scanner's RF transmission system. In addition, it can be defined as an offset from the center frequency f_0. Therefore, no check for f_0 is necessary at the start or during the procedure to set the frequency of the LARFET.

It is also possible to use the leaky 125 MHz signal from the RF transmitter of the scanner as the reference signal for frequency down-conversion. However, in this case the lower power (i.e. $FA \cong 0.2°$), may affect the SNR. But still the peaks were detectable from the noise floor and accurate localization could be achieved.

For both methods, down-conversion of the MR signal right at the source reduced the complexity and simplified the design of the later stages for signal transmission. The accuracy and precision of the system are comparable with other active tracking methods. Frequency down-conversion reduced the necessary power for the output LED and enabled the miniaturization of this system into a 1.5 mm×1.5 mm IC, which later could be mounted on catheter tips, for safe tracking of endovascular devices.

The orientation of the coil with regard to the main magnetic field B_0 can affect the signal quality and localization accuracy. Theoretically, there should be a sinusoidal relationship between the signal intensity and the angle enclosed between B_0 and the coil's main axis, where maximum signal is expected at 90° and minimum at 0°. Erhart et al. showed that this expectation is true [37]. Since in this work, only the idea of using the LARFET as the reference signal for frequency down-conversion was tested, care was taken to keep the angle large. If placed parallel to B_0, solenoid coils perform better than planar coils that are extensively proposed for tip tracking because of their

suitability for mass production and parameter repeatability. Nevertheless, it is obvious that there will be a reduction in signal quality even with solenoids. To overcome this undesired situation, different coil geometries can be applied to this system. Nonplanar coils [34] or tilted and decoupled multiple coils [65] are among the possible approaches.

Conventional active tracking systems achieve temporal resolution down to 20 ms and spatial accuracies in the order of $0.3-0.5$ mm. In this sense, the technique proposed here performs at least comparably well. The demonstrated performance together with the absence of electrical connections, we believe, paves the way for this technique to be directly applied to systems that are based on the combined nearby placement of the tip coil and circuitry for amplification and electro-optical signal conversion [50, 51, 53, 54, 66]. On the other hand, the frequency down-conversion not only simplifies the design of the stages after the LNA but also decreases the power necessary to drive the LED at the end, which is basically the electro-optical signal converter. The 'low' frequency stage is designed to have a very high gain to saturate the signal at the output and convert the sinusoidal signal into a square wave. The loss of amplitude information is not important since in our technique, only the frequency is relevant. Conversion into square waves also simplified optical transmission of the signal since square waves can turn the LED on and off. With its original frequency, an unusual high gain LNA would be necessary to drive the LED in the same manner, which is not preferable due to stability concerns. A DC offset would be necessary to turn the LED on increasing the power consumption together with the power necessary to charge and discharge parasitic capacitances at the input of the LED.

In its current form, namely, without miniaturizing the distal unit and mounting it to the tip of a catheter, the system is fully optically isolated, and while it does not adequately address the RF heating issue, it is an excellent solution to the challenges of patient isolation in which leakage currents must be limited to a total of 10 μA. In this case, if fully charged, the battery can last up to 200 hours.

The advantages of the technique we propose are as follows: 1) potentially MR safe due to optical fiber, 2) providing the device localization coordinates directly, 3)

potential high SNR due to amplification at the source, 4) maintenance of high SNR during electro-optical and opto-electrical signal conversion and transmission due to frequency down-conversion. In addition, the power necessary to drive the LED (electro-optical signal converter) is reduced with the frequency down-conversion. Hence, the limited power provided by the optical power supply (also in future IC-based designs) can be effectively used for signal amplification.

REFERENCES

1. Gerlach, W., and O. Stern, "Der experimentelle Nachweis der Richtungsquantelung im Magnetfeld," *Zeitschrift für Physik*, Vol. 9, no. 1, pp. 349–352, 1922.

2. Rabi, I. I., S. Millman, P. Kusch, and J. R. Zacharias, "The molecular beam resonance method for measuring nuclear magnetic moments the magnetic moments of Li63, Li73 and F199," *Physical Review*, Vol. 55, no. 6, pp. 526–535, 1939.

3. Bloch, F., W. W. Hansen, and M. Packard, "The nuclear induction experiment," *Physical Review*, Vol. 70, no. 7-8, pp. 474–485, 1946.

4. Arnold, J. T., S. S. Dharmatti, and M. E. Packard, "Chemical Effects on Nuclear Induction Signals from Organic Compounds," *The Journal of Chemical Physics*, Vol. 19, no. 4, p. 507, 1951.

5. Lauterbur, P. C., "Image Formation by Induced Local Interactions: Examples Employing Nuclear Magnetic Resonance," *Nature*, Vol. 242, no. 5394, pp. 190–191, 1973.

6. Garroway, A. N., P. K. Grannell, and P. Mansfield, "Image formation in NMR by a selective irradiative process," *Journal of Physics C: Solid State Physics*, Vol. 7, no. 24, pp. L457–L462, 1974.

7. Frisch, R., and O. Stern, "Über die magnetische Ablenkung von Wasserstoffmolekülen und das magnetische Moment des Protons. I," *Zeitschrift für Physikür Physik*, Vol. 85, no. 1-2, pp. 4–16, 1933.

8. Estermann, I., and O. Stern, "Über die magnetische Ablenkung von Wasserstoffmolekülen und das magnetische Moment des Protons. II," *Zeitschrift für Physikr Physik*, Vol. 86, no. 1-2, pp. 132–134, 1933.

9. Rabi, I., J. Zacharias, S. Millman, and P. Kusch, "A New Method of Measuring Nuclear magnetic Moment," *Physical Review*, Vol. 53, no. February, p. 318, 1938.

10. Gorter, C., and L. Broer, "Negative result of an attempt to observe nuclear magnetic resonance in solids," *Physica*, Vol. 9, no. 6, pp. 591–596, 1942.

11. Purcell, E., H. Torrey, and R. Pound, "Resonance Absorption by Nuclear Magnetic Moments in a Solid," *Physical Review*, Vol. 69, no. 1-2, pp. 37–38, 1946.

12. Bloch, F., "Nuclear induction," *Physical Review*, Vol. 70, no. 7-8, pp. 460–474, 1946.

13. Ernst, R. R., and W. A. Anderson, "Application of Fourier Transform Spectroscopy to Magnetic Resonance," *Review of Scientific Instruments*, Vol. 37, no. 1, p. 93, 1966.

14. Odeblad, E., and G. Lindström, "Some preliminary observations on the proton magnetic resonance in biologic samples.," *Acta Radiologica*, Vol. 43, no. 6, pp. 469–476, 1955.

15. Damadian, R., "Tumor detection by nuclear magnetic resonance.," *Science (New York, N.Y.)*, Vol. 171, no. 976, pp. 1151–1153, 1971.

16. Mansfield, P., and P. K. Grannell, "NMR 'diffraction' in solids?," *Journal of Physics C: Solid State Physics*, Vol. 6, no. 22, pp. L422–L426, 1973.

17. Mansfield, P., "Multi-planar image formation using NMR spin echoes," 1977.

18. Mansfield, P., "Real-time echo-planar imaging by NMR.," *British medical bulletin*, Vol. 40, no. 2, pp. 187–190, 1984.

19. Kumar, A., D. Welti, and R. R. Ernst, "NMR Fourier zeugmatography," *Journal of Magnetic Resonance (1969)*, Vol. 18, no. 1, pp. 69–83, 1975.

20. Razavi, R., D. L. G. Hill, S. F. Keevil, M. E. Miquel, V. Muthurangu, S. Hegde, K. Rhode, M. Barnett, J. van Vaals, D. J. Hawkes, and E. Baker, "Cardiac catheterisation guided by MRI in children and adults with congenital heart disease.," *Lancet*, Vol. 362, pp. 1877–82, Dec. 2003.

21. Duerk, J. L., E. Y. Wong, and J. S. Lewin, "A brief review of hardware for catheter tracking in magnetic resonance imaging.," *Magma*, Vol. 13, pp. 199–208, Jan. 2002.

22. Lardo, a. C., E. R. McVeigh, P. Jumrussirikul, R. D. Berger, H. Calkins, J. Lima, and H. R. Halperin, "Visualization and Temporal/Spatial Characterization of Cardiac Radiofrequency Ablation Lesions Using Magnetic Resonance Imaging," *Circulation*, Vol. 102, pp. 698–705, Aug. 2000.

23. Chung, Y. C., E. M. Merkle, J. S. Lewin, J. R. Shonk, and J. L. Duerk, "Fast T(2)-weighted imaging by PSIF at 0.2 T for interventional MRI.," *Magnetic Resonance in Medicine*, Vol. 42, pp. 335–44, Aug. 1999.

24. Bakker, C. J., R. M. Hoogeveen, J. Weber, J. J. van Vaals, M. a. Viergever, and W. P. Mali, "Visualization of dedicated catheters using fast scanning techniques with potential for MR-guided vascular interventions.," *Magnetic Resonance in Medicine*, Vol. 36, pp. 816–20, Dec. 1996.

25. Bakker, C. J., H. F. Smits, C. Bos, R. van der Weide, K. J. Zuiderveld, J. J. van Vaals, W. F. Hurtak, M. a. Viergever, and W. P. Mali, "MR-guided balloon angioplasty: in vitro demonstration of the potential of MRI for guiding, monitoring, and evaluating endovascular interventions.," *Journal of magnetic resonance imaging : JMRI*, Vol. 8, no. 1, pp. 245–50, 1998.

26. Quick, H. H., M. O. Zenge, H. Kuehl, G. Kaiser, S. Aker, S. Massing, S. Bosk, and M. E. Ladd, "Interventional magnetic resonance angiography with no strings attached: wireless active catheter visualization.," *Magnetic Resonance in Medicine*, Vol. 53, pp. 446–55, Feb. 2005.

27. Kocaturk, O., C. E. Saikus, M. a. Guttman, A. Z. Faranesh, K. Ratnayaka, C. Ozturk, E. R. McVeigh, and R. J. Lederman, "Whole shaft visibility and mechanical performance for active MR catheters using copper-nitinol braided polymer tubes.," *Journal of cardiovascular magnetic resonance*, Vol. 11, p. 29, Jan. 2009.

28. Unal, O., J. Li, W. Cheng, H. Yu, and C. M. Strother, "MR-visible coatings for endovascular device visualization.," *Journal of magnetic resonance imaging : JMRI*, Vol. 23, pp. 763–9, May 2006.

29. Omary, R. A., O. Unal, D. S. Koscielski, R. Frayne, F. R. Korosec, C. A. Mistretta, C. M. Strother, and T. M. Grist, "Real-Time MR Imaging-guided Passive Catheter Tracking with Use of Gadolinium-filled Catheters," *Journal of Vascular and Interventional Radiology*, Vol. 11, pp. 1079–1085, Sept. 2000.

30. Ratnayaka, K., A. Z. Faranesh, M. a. Guttman, O. Kocaturk, C. E. Saikus, and R. J. Lederman, "Interventional cardiovascular magnetic resonance: still tantalizing.," *Journal of cardiovascular magnetic resonance*, Vol. 10, p. 62, Jan. 2008.

31. Burl, M., G. A. Coutts, and I. R. Young, "Tuned fiducial markers to identify body locations with minimal perturbation of tissue magnetization.," *Magnetic Resonance in Medicine*, Vol. 36, pp. 491–3, Sept. 1996.

32. Weiss, S., T. Schaeffter, K. Luedeke, C. Leussler, D. Holz, K. Nehrke, V. Rasche, and R. Sinkus, "Catheter localization using a resonant fiducial marker during interactive MR fluoroscopy," in *ISMRM*, Vol. 25, p. 1954, 1999.

33. Quick, H. H., H. Kuehl, G. Kaiser, S. Bosk, J. F. Debatin, and M. E. Ladd, "Inductively coupled stent antennas in MRI," *Magnetic Resonance in Medicine*, Vol. 48, pp. 781–790, Nov. 2002.

34. Busse, H., G. Thörmer, N. Garnov, J. Haase, T. Kahn, and M. Moche, "Technique for wireless position tracking of intravascular catheters : Performance evaluation in a vessel phantom," in *ISMRM*, Vol. 18, p. 4163, 2010.

35. Hurst, G. C., J. Hua, J. L. Duerk, and A. M. Cohen, "Intravascular (catheter) NMR receiver probe: Preliminary design analysis and application to canine iliofemoral imaging," *Magnetic Resonance in Medicine*, Vol. 24, pp. 343–357, Apr. 1992.

36. Ladd, M. E., G. G. Zimmermann, G. C. McKinnon, G. K. von Schulthess, C. L. Dumoulin, R. D. Darrow, E. Hofmann, and J. F. Debatin, "Visualization of vascular guidewires using MR tracking.," *Journal of magnetic resonance imaging : JMRI*, Vol. 8, no. 1, pp. 251–3, 1998.

37. Erhart, P., M. E. Ladd, P. Steiner, N. Heske, C. L. Dumoulin, and J. F. Debatin, "Tissue-independent MR tracking of invasive devices with an internal signal source.," *Magnetic Resonance in Medicine*, Vol. 39, pp. 279–84, Feb. 1998.

38. Dumoulin, C. L., S. P. Souza, and R. D. Darrow, "Real-time position monitoring of invasive devices using magnetic resonance.," *Magnetic Resonance in Medicine*, Vol. 29, pp. 411–5, Mar. 1993.

39. Ozturk, C., M. Guttman, E. R. McVeigh, and R. J. Lederman, "Magnetic resonance imaging-guided vascular interventions.," *Topics in magnetic resonance imaging : TMRI*, Vol. 16, no. 5, pp. 369–381, 2005.

40. Guttman, M. a., C. Ozturk, A. N. Raval, V. K. Raman, A. J. Dick, R. DeSilva, P. Karmarkar, R. J. Lederman, and E. R. McVeigh, "Interventional cardiovascular procedures guided by real-time MR imaging: an interactive interface using multiple slices, adaptive projection modes and live 3D renderings.," *Journal of magnetic resonance imaging : JMRI*, Vol. 26, pp. 1429–35, Dec. 2007.

41. Wacker, F. K., D. Elgort, C. M. Hillenbrand, J. L. Duerk, and J. S. Lewin, "The catheter-driven MRI scanner: a new approach to intravascular catheter tracking and imaging-parameter adjustment for interventional MRI.," *AJR. American journal of roentgenology*, Vol. 183, pp. 391–5, Aug. 2004.

42. Bock, M., S. Volz, S. Zühlsdorff, R. Umathum, C. Fink, P. Hallscheidt, and W. Semmler, "MR-guided intravascular procedures: real-time parameter control and automated slice positioning with active tracking coils.," *Journal of magnetic resonance imaging : JMRI*, Vol. 19, pp. 580–9, May 2004.

43. Hillenbrand, C. M., D. R. Elgort, E. Y. Wong, A. Reykowski, F. K. Wacker, J. S. Lewin, and J. L. Duerk, "Active device tracking and high-resolution intravascular MRI using a novel catheter-based, opposed-solenoid phased array coil.," *Magnetic Resonance in Medicine*, Vol. 51, pp. 668–75, Apr. 2004.

44. Nitz, W. R., a. Oppelt, W. Renz, C. Manke, M. Lenhart, and J. Link, "On the heating of linear conductive structures as guide wires and catheters in interventional MRI.," *Journal of magnetic resonance imaging : JMRI*, Vol. 13, pp. 105–14, Jan. 2001.

45. Yeung, C. J., and E. Atalar, "A Green's function approach to local rf heating in interventional MRI.," *Medical physics*, Vol. 28, pp. 826–32, May 2001.

46. Vernickel, P., V. Schulz, S. Weiss, and B. Gleich, "A safe transmission line for MRI.," *IEEE transactions on bio-medical engineering*, Vol. 52, pp. 1094–102, June 2005.

47. Weiss, S., P. Vernickel, T. Schaeffter, V. Schulz, and B. Gleich, "Transmission line for improved RF safety of interventional devices.," *Magnetic Resonance in Medicine*, Vol. 54, pp. 182–9, July 2005.

48. Bottomley, P. a., A. Kumar, W. a. Edelstein, J. M. Allen, and P. V. Karmarkar, "Designing passive MRI-safe implantable conducting leads with electrodes," *Medical Physics*, Vol. 37, p. 3828, July 2010.

49. Sonmez, M., C. E. Saikus, J. a. Bell, D. N. Franson, M. Halabi, A. Z. Faranesh, C. Ozturk, R. J. Lederman, and O. Kocaturk, "MRI active guidewire with an embedded temperature probe and providing a distinct tip signal to enhance clinical safety.," *Journal of cardiovascular magnetic resonance*, Vol. 14, p. 38, Jan. 2012.

50. Fandrey, S., S. Weiss, and J. Muller, "Development of an active intravascular MR device with an optical transmission system.," *IEEE transactions on medical imaging*, Vol. 27, pp. 1723–7, Dec. 2008.

51. Fandrey, S., S. Weiss, and J. Müller, "A novel active MR probe using a miniaturized optical link for a 1.5-T MRI scanner.," *Magnetic Resonance in Medicine*, Vol. 67, pp. 148–55, Jan. 2012.

52. Pitsaer, C., R. Umathum, A.-K. Homagk, C. Ozturk, and M. Bock, "Three concepts for tuning and matching intravascular catheter coils," in *ISMRM*, Vol. 18, p. 1852, 2010.

53. Anders, J., P. Sangiorgio, X. Deligianni, F. Santini, K. Scheffler, and G. Boero, "Integrated active tracking detector for MRI-guided interventions.," *Magnetic Resonance in Medicine*, Vol. 67, pp. 290–6, Jan. 2012.

54. Sarioglu, B., O. Aktan, A. Oncu, S. Mutlu, G. Dundar, and A. D. Yalcinkaya, "An Optically Powered CMOS Receiver System for Intravascular Magnetic Resonance Applications," *IEEE Journal on Emerging and Selected Topics in Circuits and Systems*, Vol. 2, pp. 683–691, Dec. 2012.

55. Tümer, M., B. Sarioglu, S. Mutlu, A. Yalcinkaya, and C. Ozturk, "LARFET (Low Amplitude RF at Echo Time) for Catheter Tracking," in *ISMRM*, Vol. 21, p. 1838, 2013.

56. Tümer, M., B. Sarioglu, S. Mutlu, Y. Ulgen, A. Yalcinkaya, and C. Ozturk, "Using a low-amplitude RF pulse at echo time (LARFET) for device localization in MRI," *Medical & Biological Engineering & Computing*, Vol. 52, no. 10, pp. 885–894, 2014.

57. Bloch, F., and A. Siegert, "Magnetic resonance for nonrotating fields," *Physical Review*, Vol. 57, no. 1939, pp. 522–527, 1940.

58. Ramsey, N., "Resonance transitions induced by perturbations at two or more different frequencies," *Physical Review*, Vol. 100, pp. 1191–4, Feb. 1955.

59. Linte, C. a., P. Lang, M. E. Rettmann, D. S. Cho, D. R. Holmes, R. a. Robb, and T. M. Peters, "Accuracy considerations in image-guided cardiac interventions: experience and lessons learned.," *International journal of computer assisted radiology and surgery*, Vol. 7, pp. 13–25, Jan. 2012.

60. Fritz, J., P. U-Thainual, T. Ungi, A. J. Flammang, N. B. Cho, G. Fichtinger, I. I. Iordachita, and J. a. Carrino, "Augmented reality visualization with image overlay for MRI-guided intervention: accuracy for lumbar spinal procedures with a 1.5-T MRI system.," *AJR. American journal of roentgenology*, Vol. 198, pp. W266–73, Mar. 2012.

61. Folltills, U., R. Baumgartl, F. Schmitt, G. Pirkl, and B. Stoeckel, "Magnetic Resonance Transmission Array," 2008.

62. Baumgartl, R., M. Buettner, G. Pirkl, and A. Potthast, "Magnetic Resonance Apparatus with Structurally Separate RF Transmit and RF Reception Devices," 2011.

63. Sarioglu, B., M. Tümer, U. Cindemir, B. Camli, G. Dundar, C. Ozturk, and A. D. Yalcinkaya, "An Optically Powered CMOS Tracking System for 3 T Magnetic Resonance Environment," *IEEE Transactions on Biomedical Circuits and Systems*, Vol. 9, no. 1, pp. 12–20, 2015.

64. Bushberg, J. T., J. A. Seibert, E. M. Leidholdt Jr, and J. M. Boone, *The Essential Physics of Medical Imaging*, Philadelphia: Lippincott Williams & Wilkins, 2 ed., 2002.

65. Kuehne, T., R. Fahrig, and K. Butts, "Pair of resonant fiducial markers for localization of endovascular catheters at all catheter orientations.," *Journal of magnetic resonance imaging : JMRI*, Vol. 17, pp. 620–4, May 2003.

66. Sun, N., Y. Liu, H. Lee, R. Weissleder, D. Ham, and S. Member, "CMOS RF Biosensor Utilizing Nuclear Magnetic Resonance," *IEEE Journal of Solid-State Circuits*, Vol. 44, pp. 1629–1643, May 2009.